nature communications

Article

https://doi.org/10.1038/s41467-025-59402-0

Saddle curvature association of nsP1 facilitates the replication complex assembly of Chikungunya virus in cells

Received: 2 December 2024

Accepted: 22 April 2025

Published online: 08 May 2025

Check for updates

Xinwen Miao[1], Michelle Cheok Yien Law[2,3], Jatin Kumar[4], Choon-Peng Chng[4], Yongpeng Zeng[1], Yaw Bia Tan[2,3], Jiawei Wu[1,5], Xiangfu Guo[1], Lizhen Huang[1], Yinyin Zhuang[1], Weibo Gao[6,7], Changjin Huang[4] ✉, Dahai Luo[2,3,8] ✉ & Wenting Zhao[1,9] ✉

Positive-sense RNA viruses, including SARS-CoV-1 and -2, DENV, and CHIKV, replicate in curved membrane compartments within host cells. Non-structural proteins (nsPs) critically regulate these nanoscale membrane structures, yet their curvature-dependent assembly remains elusive due to the challenges of imaging nanoscale interaction on curved surfaces. Using vertically aligned nanostructures to generate pre-defined membrane curvatures, we here investigate the impact of curvature on nsPs assembly. Taking CHIKV as a model, we reveal that nsP1 preferentially binds and stabilizes on positively curved membranes, with stronger accumulation at radii ≤150 nm. This is driven by hydrophobic residues in the membrane association (MA) loops of individual nsP1. Molecular dynamics simulations further confirm the improved binding stability of nsP1 on curved membranes, particularly when it forms a dodecamer ring. Together, nsP1 supports a strong saddle curvature association, with flexible MA loops sensing a range of positive curvatures in the x-z plane while the rigid dodecamer stabilizing fixed negative curvature in the x-y plane - crucial for constraining the membrane spherule neck during replication progression. Moreover, CHIKV replication enriches on patterned nanoring structures, underscoring the curvature-guided assembly of the viral replication complex. Our findings highlight membrane curvature as a key regulator of viral nsPs organization, opening new avenues for studying membrane remodeling in viral replication.

Many positive-strand RNA viruses generate nanoscale confined membrane compartments dedicated to protecting and facilitating their genome replication. These include highly pathogenic viruses like hepatitis C virus (HCV)[1], chikungunya virus (CHIKV)[2], dengue virus (DENV)[3], Zika virus (ZIKV)[4], the severe acute respiratory syndrome coronavirus (SARS-CoV)[5], and the latest SARS-CoV-2[6] causing the COVID-19 pandemic. Such viral replication-associated membrane compartments have been found in various structures composed of

[1]School of Chemistry, Chemical Engineering and Biotechnology, Nanyang Technological University, Singapore, Singapore. [2]Lee Kong Chian School of Medicine, Nanyang Technological University, Singapore, Singapore. [3]NTU Institute of Structural Biology, Nanyang Technological University, Singapore, Singapore. [4]School of Mechanical and Aerospace Engineering, Nanyang Technological University, Singapore, Singapore. [5]State Key Laboratory Breeding Base of Green Chemistry Synthesis Technology, College of Chemical Engineering, Zhejiang University of Technology, Hangzhou, China. [6]School of Electrical & Electronic Engineering, Nanyang Technological University, Singapore, Singapore. [7]School of Physics and Mathematical Science, Nanyang Technological University, Singapore, Singapore. [8]National Centre for Infectious Diseases, Singapore, Singapore. [9]Institute for Digital Molecular Analytics and Science, Nanyang Technological University, Singapore, Singapore. ✉e-mail: cjhuang@ntu.edu.sg; luodahai@ntu.edu.sg; wtzhao@ntu.edu.sg

either double- or single-membrane vesicles, ranging from tens to hundreds of nanometers[7], and extending from diverse cellular membranes including both the plasma membrane (PM) at the cell surfaces[8] and intracellular organelles like the endoplasmic reticulum (ER)[9], mitochondria[10], endosomes[11], lysosomes[12], and peroxisomes[13]. However, how viruses hijack the host cell membrane to assemble specific nanoscale membrane compartments for their own purposes is largely unclear. These membrane compartments are usually associated with viral replication complexes (RCs) formed by non-structural proteins (nsPs), together with unknown host factors in many cases, to help RNA synthesis[2,14]. Among them, only a handful of nsPs are responsible for binding and remodeling the host cell membrane[15]. They act on a variety of membrane shapes, i.e., from highly curved ER tubular networks[16] to spherule-shaped mitochondria[10] and PM[8]. Geometrically, nsPs are also found on multiple curvature types, including not only the positive and negative curvature in a 2D plane[17,18] but also the unique saddle curvature in 3D[2,14]. One intriguing yet unexplored question is whether, or how, the existing curvatures predispose or modulate the recruitment and organization of nsPs for membrane remodeling during viral replication.

Various technologies have been explored to study the nanoscale assembly of viral nsPs on host cell membranes. Electron microscopy (EM) is the most popular method to visualize host cell membranes remodeled by viral nsPs with nanometer resolution[3,9,11]. However, the location of viral nsPs is poorly resolved with immunogold labeling, and no dynamic correlation between protein and membrane curvature is achievable. Transient expression of fluorescent-tagged viral nsPs in host cells has been widely used to examine their dynamic distribution on[19,20] or co-localization with various intracellular organelles[21,22]. Unfortunately, the formation of nanoscale membrane compartments is often below the optical resolution of fluorescence microscopy and thus is hardly resolved beyond diffraction-limited puncta. Liposome binding and co-floating assays are used to measure nsPs' binding affinity to the curved vesicles in vitro[23,24], where the binding-related protein conformational changes can also be measured by circular dichroism (CD) spectroscopy[25], and the resulting membrane deformation, if any, is visualized by TEM[25–27]. However, whether the in vitro behaviors reflect the native viral RCs assembled in live cells needs to be validated. Recently, direct manipulation of nanoscale membrane curvature in cells has been achieved using nanostructure-based surface engineering assay[28–35] and optical tweezer-based membrane tethering assays[36–38]. These approaches have demonstrated that nanoscale membrane curvature can influence various cellular processes - enhancing the accumulation of endocytic proteins[28,32], Ras clustering[30], G protein-coupled receptors[30,36], glycoproteins[33], Bin/Amphiphysin/Rvs (BAR) proteins[39], and Wiskott–Aldrich syndrome protein (WASP)[35], as well as facilitating actin polymerization[29] and integrin-mediated adhesions[34]. Nevertheless, whether it can be applicable to investigate viral replication has yet to be demonstrated.

Here, we fabricate vertically aligned nanostructure arrays with various designed geometries to provide both positively and negatively curved PM sites with defined nanoscale curvature values in live cells. This platform allows for the survey of a range of curvature values and signs that are likely present at different stages during the progressive formation of highly curved membrane spherules from relatively flat membranes. Taking CHIKV as a model, we probe the distribution of its membrane-targeting nsP1 on both positively and negatively curved membranes. The impact of lipid composition and different protein domains is examined in live cells and validated in vitro using supported lipid bilayers (SLBs) formed on the nanostructures. All-atom and coarse-grained simulations are performed to evaluate the contribution of curvature to the binding and stabilization of nsP1 on the membrane. Furthermore, membrane curvature-guided viral RC assembly in infected cells is successfully demonstrated using patterned nanostructure arrays.

Results and discussion

Positive curvature-promoted membrane association of CHIKV nsP1 in live cells

Different from other alphaviruses that generate spherules on the PM during the early stage of infection and later internalize them into cytopathic vacuoles, the membrane spherules for CHIKV replication are mainly observed on the PM throughout infection[8,40]. Among the four nsPs of CHIKV that are needed for the membrane spherule formation on the PM, nsP1 is the only one known to associate with the membrane, serving as the critical link to connect the PM and CHIKV RC assembly[19,41,42]. Yet, how the local PM curvature affects the membrane association of nsP1 in live cells, and consequently, the viral genome replication is largely unknown.

The recent cryo-electron tomography (cryo-ET) study showed that nsPs precisely assembled at the neck of the membrane spherules, where a unique saddle curvature geometry (Fig. 1a, left column) was formed, combining positive curvature (x-z plane) and negative curvature (x-y plane) in 3D[2,14]. An intriguing question is whether the nsPs prefer binding to positive or negative curvature or both at the same time, but via different planes. However, it is technically challenging to image the 3D saddle curvature at the nanoscale due to the limited microscopy resolution. To better dissect the interaction of nsP1 with this unique saddle structure, we designed two types of nanostructures to decouple 3D saddle curvature into two 2D curvatures (Fig. 1a, middle & right columns; Fig. 1b). Specifically, the positive curvature at the x-z plane of the saddle point was recapitulated by the positively curved nanobar ends in the x-y plane (Fig. 1a, top row), while the negative curvature at the x-y plane of the saddle point was recapitulated by the negatively curved intersection of a nanocross design in the x-y plane as well (Fig. 1a, bottom row). This reorientation of both positive and negative curvatures into the x-y plane allowed better resolution to measure the curvature-guided nsP1 accumulation on the PM.

We first examined the curvature preference of nsP1 alone using transiently expressed eGFP tagged nsP1 (eGFP-nsP1) in U2OS cells plated on nanobar and nanocross arrays (Fig. 1b). Both nanostructures have a height of 600 nm and a length of 2 μm, with widths of 250 nm for nanobars and 350 nm for nanocrosses (scanning electron microscopy (SEM) images in Fig. 1b). These dimensions are significantly larger than the ~ 20 nm diameter of the nsP1 dodecamer[14], ensuring no physical constraint preventing nsP1 from accessing any site on the nanostructure surface. Interestingly, eGFP-nsP1 exhibited a significant preference for the positively curved membranes at the nanobar ends, as shown in both representative images (Fig. 1c) and average images (Fig. 1d), where the protein density at the two curved nanobar ends was significantly higher than at the flat center. This curvature sensing ability of eGFP-nsP1 was mainly attributable to nsP1, rather than the fluorescence tag, as the expression of GFP alone exhibited a strong cytosolic signal and lacked the ability to associate with the PM (Supplementary Fig. 1). To evaluate the curvature preference of nsP1, we quantified the fluorescence intensity at the nanobar end versus the nanobar center, indicated as 'end-to-center ratio' (Fig. 1e). A significant difference between CellMask-stained membrane (1.233 ± 0.637, mean ± SD [standard deviation]) and eGFP-nsP1 (2.129 ± 1.718) was observed (two-tailed unpaired t test, $P < 0.0001$). The cumulative frequency distribution of the end-to-center ratio also showed a similar trend that more than 72% of nsP1-bound nanobars displayed a ratio greater than 1 while only 36% were observed in the CellMask labeled ones (Supplementary Fig. 2). Super-resolution imaging with stimulated emission depletion microscopy (STED) further confirmed that multiple nsP1 puncta were enriched at the positively curved nanobar ends (Supplementary Fig. 3). In comparison, eGFP-nsP1 exhibited no detectable enrichment at the negatively curved nanocross intersection but showed strong accumulation at the positively curved corners of the nanocross arms. (Fig. 1f, g). These results suggested that, although

https://doi.org/10.1038/s41467-025-59402-0

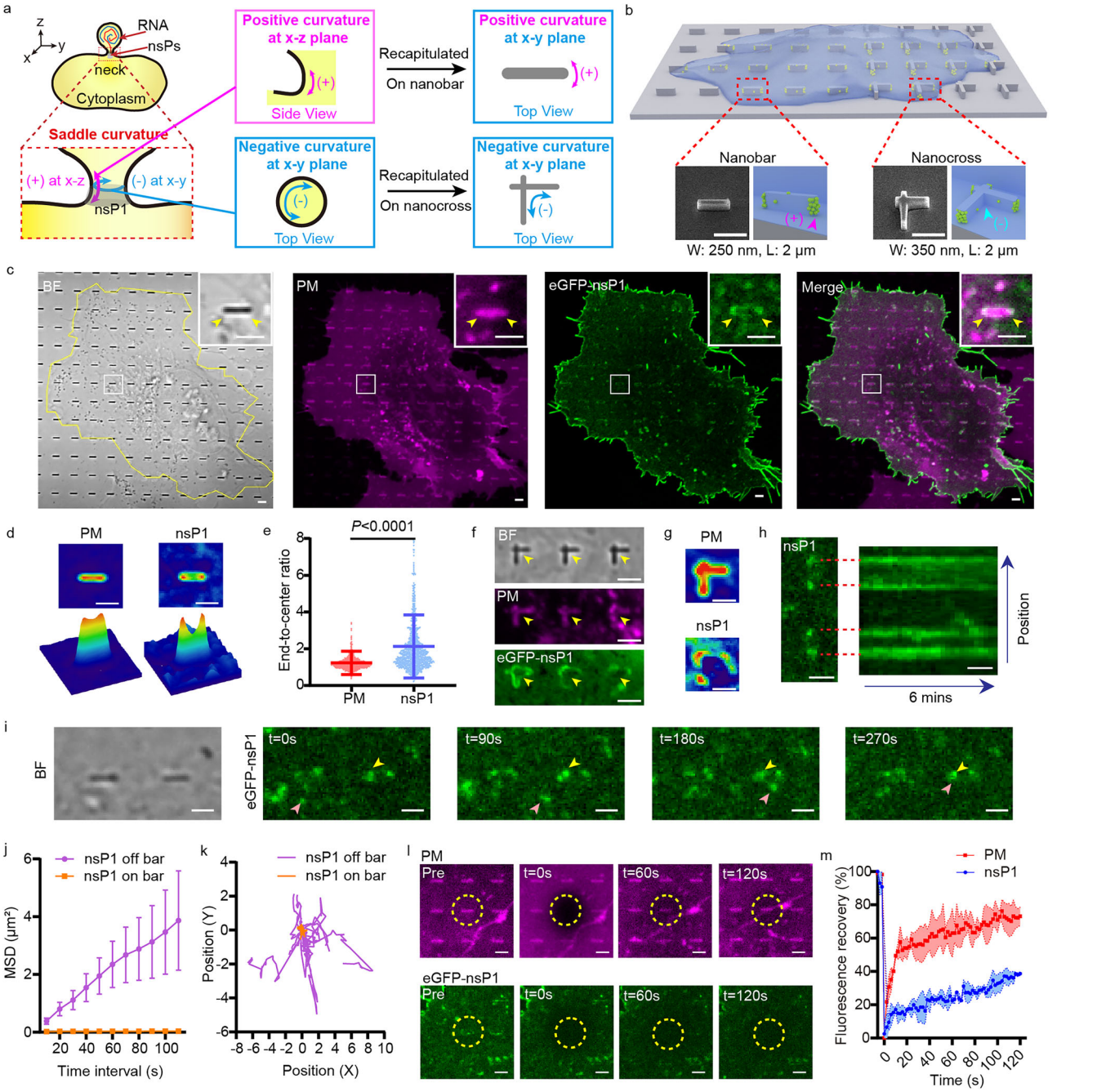

Fig. 1 | CHIKV nsP1 curvature sensing ability on nanostructures in live cells. **a** Schematic of a spherule on the plasma membrane (PM). The neck displays saddle curvature: positive (+) in the x-z plane and negative (-) in the x-y plane. Two types of nanostructures were designed to recapitulate the 3D saddle curvature into 2D. **b** Illustration and SEM image of the nanostructures: both 600 nm in height and 2 μm in length. The nanobar is 250 nm wide (pink arrow indicates positive curvature), and the nanocross is 350 nm wide (blue arrow indicates negative curvature). **c** U2OS cells cultured on nanobars with CellMask-stained PM (magenta) and overexpressed eGFP-nsP1 (green). The cell boundary shown in brightfield. $n = 3$ repeats. **d** Average images and 3D surface plots of PM ($n = 489$ bars) and eGFP-nsP1 ($n = 223$ bars) distribution around nanobars. **e** The end-to-center ratio of PM ($n = 995$) and eGFP-nsP1 ($n = 1005$) on nanobars. Mean ± SD [standard deviation]. **f** Cells cultured on nanocrosses with CellMask-stained PM (magenta) and overexpressed eGFP-nsP1 (green). Yellow arrows indicate negatively curved areas. $n = 3$ repeats. **g** Average images of PM and eGFP-nsP1 distribution around nanocrosses ($n = 33$ crosses). **h** Kymograph plots of eGFP-nsP1 on two adjacent nanobars. **i** Time-lapse images of eGFP-nsP1 clusters on (yellow arrows) and off (pink arrows) nanobars over 270 s. **j** Mean square displacement (MSD) of eGFP-nsP1 clusters on ($n = 14$) and off ($n = 12$) the nanobars in 110 s. Mean ± SEM [standard error of the mean]. **k** The trajectory of nsP1 clusters on ($n = 14$) and off ($n = 12$) bars over 110 s. **l** Confocal images of fluorescence recovery after photobleaching (FRAP) test for PM (magenta) and eGFP-nsP1 (green) on nanobar over 120 s. Yellow dashed circles indicate the bleached area. $n = 3$ repeats. **m** Normalized fluorescence intensity plot of PM and eGFP-nsP1 within nanobar area from FRAP measurement (2 s interval). Mean ± SD. Statistical analysis: two-tailed unpaired t test. Scale bars: 2 μm. Source data are provided as a Source Data file.

the neck of the spherule presented both positive and negative curvature sites, the assembly of nsP1 and other associated nsPs could be more dominantly affected by how curved the membrane was toward a positive direction. It is worth noting that nsP1 was also observed to accumulate inside filopodia-like protrusion structures in cells. However, recent cryo-ET studies showed that these filopodia-like structures could not generate membrane spherules for CHIKV replication[2,14], but were coupled with other host factors like Rac1-PAK1-Arp2/3 signaling[43], thus less relevant to study here for the impact of curvature on spherule formation. Interestingly, we observed that CHIKV replication preferentially accumulated at the positively curved membrane of the host cells, compared to the nearby protruded areas with negatively curved membranes (Supplementary Fig. 4), suggesting an important influence of positive curvature on CHIKV replication.

Besides the curvature-guided spatial distribution of nsP1 on the membrane, we also examined its temporal stability at curved sites. By taking a six-minute time series of eGFP-nsP1 on nanobar arrays (Supplementary Movie 1), we found that the nsP1 puncta were persistently associated with nanobar ends without significant intensity decay. The kymography analysis in Fig. 1h similarly showed that the nsP1 intensity dominated at the nanobar ends with very little signal along the flat nanobar centers, indicating that the preferential association of nsP1 at the curved membrane sites was stable over time. In addition, snapshots of the nsP1 puncta at the nanobar ends also showed minimal lateral movement while those on the surrounding flat membrane could still move around (Fig. 1i), resulting in significantly lower mean square displacement (MSD) (Fig. 1j) and shorter trajectories of the nsP1 puncta over time (Fig. 1k). The temporal analysis strongly suggested that the highly curved nanobar end could stabilize nsP1 around it. Interestingly, when we performed a fluorescence recovery after photobleaching (FRAP) test on the fluorescence signals of both eGFP-nsP1 and CellMask at the nanobar ends, there was no detectable recovery observed for nsP1, but the membrane signal recovery remained normal (Fig. 1l, m; Supplementary Movie 2). It suggests that nsP1 is strongly anchored at the curved PM sites with no detectable lateral diffusion and dynamic assembly.

Since the nsPs of the *alphavirus* genus are relatively conserved and share ~60–80% sequence homology[44–46], we further validated the curvature-guided membrane assembly of nsP1 using another virus in the same genus, Venezuelan equine encephalitis virus (VEEV). Similar to CHIKV nsP1, VEEV nsP1 also showed a stronger membrane association at the nanobar ends than at the center (Supplementary Fig. 5a, b). The end-to-center ratio of VEEV nsP1 was not significantly different compared to CHIKV (Supplementary Fig. 5c, CHIKV: 2.018 ± 1.871 *vs.* VEEV: 1.878 ± 1.505, two-tailed unpaired *t* test, $P = 0.1127$), with 48% of the values greater than 1 (Supplementary Fig. 5d). These data indicate that the positive curvature-promoted membrane association of nsP1 is not specific to CHIKV only, but a conserved behavior among multiple alphaviruses for facilitating the viral replication process.

Recapitulating the curvature-dependent membrane association of CHIKV nsP1 in vitro

The positive curvature-guided membrane association of nsP1 was further validated by examining purified nsP1 on synthetic lipid bilayers formed in vitro on nanobar arrays, as illustrated in Fig. 2a. Here, eGFP-fused nsP1 protein was purified from the *E. coli* protein expression system (eGFP-nsP1-(b) for short) to obtain the monomeric fraction[44]. SLB containing 89.5% phosphatidylcholine (from egg, egg PC for short), 10% phosphatidylserine (from brain, brain PS for short), and 0.5% Texas Red™ 1,2-Dihexadecanoyl-sn-Glycero-3-Phosphoethanolamine (Texas Red-PE) was formed on the surface of the nanobar and then incubated with eGFP-nsP1-(b). Interestingly, eGFP-nsP1-(b) monomer showed not only strong membrane binding as reported earlier[25], but also preferential accumulation at curved membrane sites at nanobar ends (Fig. 2b). The curvature preference was more clearly observed in both averaged images (Fig. 2c) and quantified end-to-center ratio (eGFP-nsP1: 1.109 ± 0.106 *vs.* lipid: 1.018 ± 0.121, two-tailed unpaired *t* test, $P < 0.0001$) (Fig. 2d). It indicates that nsP1 senses the membrane curvature on its own without the need for other viral materials and/or host factors.

To examine the range of membrane curvature that CHIKV nsP1 senses, we employed a nanobar array with a curvature gradient, with the half-circle diameter ranging from 100 nm to 600 nm in 100 nm increments (SEM images shown in Fig. 2e). The purified eGFP-nsP1-(b) exhibited stronger binding to smaller nanobars than to the larger ones, as shown in both representative images (Supplementary Fig. 6) and the averaged ones (Fig. 2f). The protein density at differently sized nanobar ends was calculated by the ratio of nsP1 intensity at the nanobar end over the lipid fluorescence intensity per unit area. By plotting the normalized bar-end density across different nanobar diameters, we observed that the higher the membrane curvature was generated, the higher the protein density was obtained (Fig. 2g). Especially when the membrane was deformed with curvature corresponding to a diameter less than 300 nm, the nsP1 demonstrated increasing curvature-dependent binding preference as the curvature diameter decreased. This suggestes that during the formation of viral membrane spherule, the progressive increase in positive membrane curvature formed in the x-z plane of the saddle curvature enhances nsP1 accumulation on the membrane. However, different from the low FRAP recovery (~20%) of mammalian-expressed nsP1 on live cell PM (Fig. 1l, m), the bacteria-expressed eGFP-nsP1-(b) showed much higher recovery (~70%) on SLB-coated nanobars after photobleaching (Fig. 2h, i; Supplementary Movie 3), demonstrating higher mobility on the membrane. Considering the fact that no post-translational modification exists in the bacterial expression system, eGFP-nsP1-(b) used in vitro here lacks the S-palmitoylation at the cysteine residues. Earlier work reported that the S-palmitoylation directed nsP1 to cholesterol-rich regions on the cell membrane[47]. Therefore, the absence of both cholesterol in the SLB and S-palmitoylation on eGFP-nsP1-(b) here could lead to the observed increase in mobility.

The impact of membrane charges on the curvature-dependent membrane binding of nsP1 was also evaluated. Recent studies have shown that negatively charged lipids enhanced the membrane binding of nsP1 via electrostatic interaction[2,25,42]. However, whether or how it affects the curvature sensitivity of nsP1 is unknown. Here, we measured nsP1 binding on nanobar-curved SLBs containing negatively charged 16:0-18:1 phosphatidylserine (POPS) at different concentrations (0%, 30%, and 50%) (Fig. 2j–l). Consistent with prior studies using liposomes and giant unilamellar vesicles[2,25], nsP1 poorly bound to neutrally charged SLB with 16:0-18:1 phosphatidylcholine (POPC) only as evidenced by low fluorescence intensity across all the nanobar structures (Fig. 2j). With the increase of POPS from 30% to 50%, nsP1 showed higher fluorescence intensity both on nanobars and on the flat areas in between (Fig. 2j), confirming the electrostatics-dependent membrane binding of nsP1. The relative protein density measured on nanobars increased significantly from 0% POPS (0.079 ± 0.036) to 30% POPS (0.448 ± 0.145) and 50% POPS (0.642 ± 0.192) (Fig. 2k). However, the normalized protein density at the nanobar end exhibited no significant difference across all the nanobar dimensions (Fig. 2l), indicating a minor influence of membrane charges across the range of curvatures that nsP1 can sense.

In addition to PS, we also examined another negatively charged lipid, 16:0-18:1 phosphatidic acid (PA) in vitro (Supplementary Fig. 7a), which is also anionic but with smaller head groups than PS. Similar to the effect of PS, higher PA concentration resulted in an increase of binding density of nsP1 on SLB (Supplementary Fig. 7b), but not in sensitivity to different curvature values (Supplementary Fig. 7c). However, comparing the results of PS and PA at the same concentration (30%), it was interesting to note that nsP1 enriched more on PA- than PS- containing SLB (Supplementary Fig. 7d). This is likely due to the fact that PA has a smaller headgroup than PS and thus offers more lipid packing defects at the curved membrane for

https://doi.org/10.1038/s41467-025-59402-0

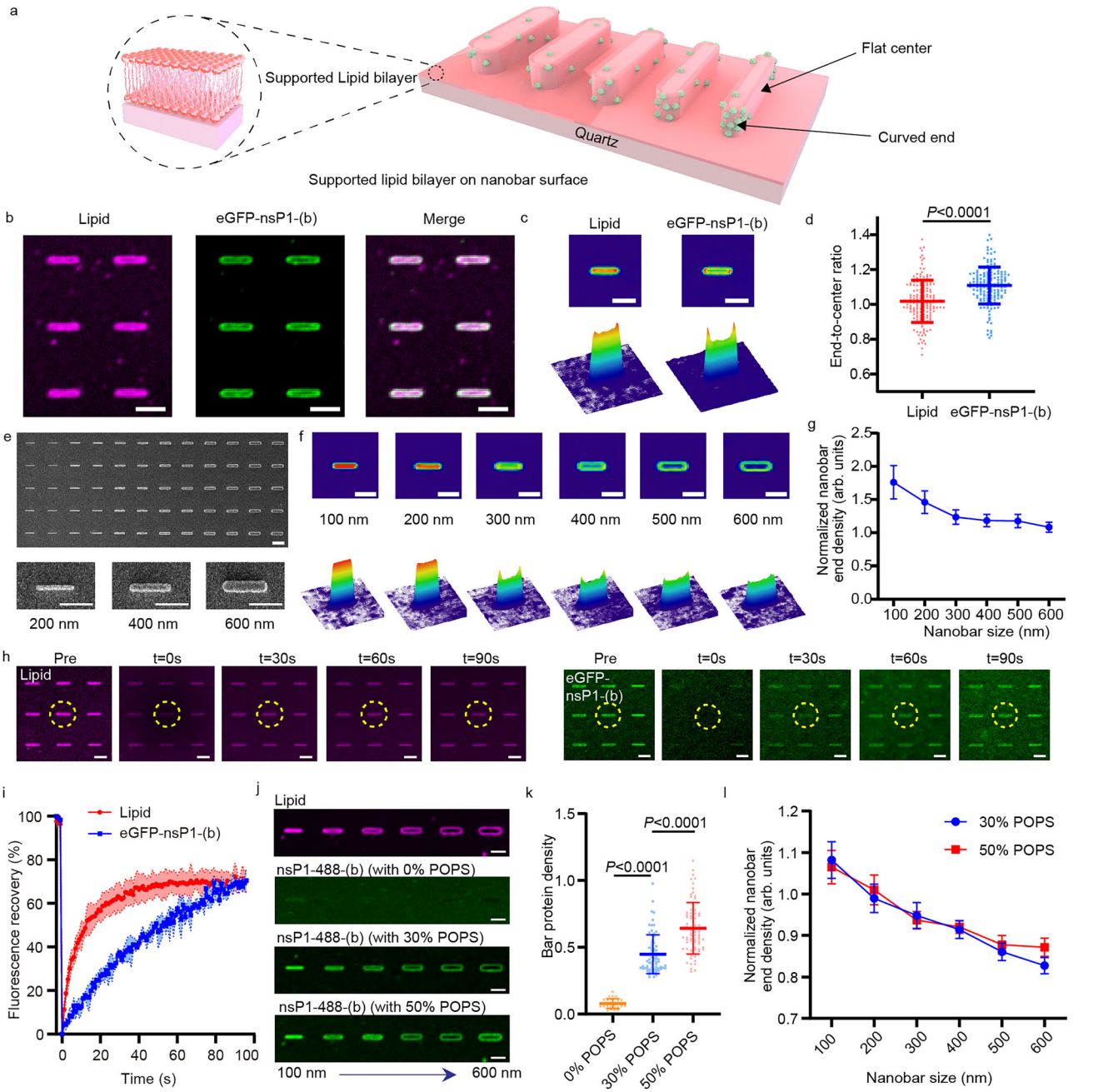

Fig. 2 | Bacterial expressed CHIKV nsP1 curvature sensing ability on supported lipid bilayer (SLB). a Illustration of SLB wrapping around nanobars with increasing widths. Curvature-sensing proteins preferentially bind to highly curved ends of smaller nanobars. **b** Confocal images showing uniform SLB (magenta) on 300 nm-wide nanobars, with 5.4 μM bacterial expressed nsP1 (eGFP-nsP1-(b); green) bound to the bilayer. $n = 3$ repeats. **c** Average images and 3D surface plots of the SLB and eGFP-nsP1-(b) on 300 nm-wide nanobars ($n = 58$ bars). **d** The end-to-center ratio of the SLB and eGFP-nsP1-(b) on 300 nm-wide nanobars ($n = 164$). Mean ± SD. **e** SEM image of nanobar arrays with widths from 100 nm to 600 nm (two columns, one size). The lower panel shows bars with 200, 400, and 600 nm widths. $n = 3$ repeats. **f** Average images and 3D surface plots of eGFP-nsP1-(b) on 100–600 nm nanobars over 80 bars. **g** Normalized nanobar-end density of eGFP-nsP1-(b) on 100–600 nm nanobars over 80 bars. Mean ± SEM. **h** Confocal FRAP images of SLB (magenta) and eGFP-nsP1-(b) (green) on 200 nm nanobars over 90 s. Yellow dashed circles indicate the bleached area. $n = 3$ repeats. **i** Normalized fluorescence intensity plot of SLB and nsP1 within nanobar area from FRAP measurement (2 s interval). Mean ± SD. **j** Confocal images of SLB (magenta) and 1 μM Alexa Fluor 488-labeled nsP1 (nsP1-(488)-(b); green) on gradient nanobars with 0% POPS, 30% POPS, or 50% POPS lipid compositions. $n = 3$ repeats. **k** Relative nsP1 protein density across different lipid compositions over 80 bars. Mean ± SD. **l** Normalized nanobar-end density of nsP1-(488)-(b) on 100–600 nm nanobars coated with 30% and 50% POPS SLBs over 80 bars. Mean ± SEM. Statistical analysis: two-tailed unpaired t test. Scale bars: 2 μm. Arb. units = arbitrary units. Source data are provided as a Source Data file.

the curvature-sensitive protein to bind[48]. Overall, our results here demonstrate that the geometry of lipid molecules has a stronger impact on the curvature sensitivity of nsP1 than their charges, although negatively charged lipids are necessary to ensure sufficient binding density of nsP1 on the membrane.

Hydrophobic residues of CHIKV nsP1 are essential for curvature sensing

To understand the curvature sensing mechanism of CHIKV nsP1, we further examined the role of several characteristic domains reported earlier for membrane binding in CHIKV or its closely related Semliki

Forest virus (SFV) in the *alphavirus* genus. These included two recently identified membrane association (MA) loops around amino acids (a.a.) 220–233 (MA loop 1) and a.a. 407 to 427 (MA loop 2)[44,49], a palmitoylation site at a.a. 417–419 near the C-terminus[47], and an amphipathic helix (AH)[25] corresponding to a.a. 244–263 that was previously demonstrated for effective membrane deformation in vitro and affecting the membrane association in cells for SFV (Fig. 3a; the nsP1 model structure was predicted using AlphaFold[50], and the visualization was generated using PyMOL). It is worth noting that, although the AH of CHIKV nsP1 was recently revealed as non-critical for its membrane binding, it was still included here as an important control to exclude any potential influence of it on nsP1's curvature-sensing ability. This is because curvature sensing is not equivalent to membrane binding and can be altered via weaker molecular interactions[51] than the stronger affinity needed for membrane binding. Accordingly, a series of mutations targeting these domains individually or combinatorically were constructed for evaluation, together with two truncations removing the flexible regions that have not been structurally resolved (a.a. 476–516 and a.a. 516–535)[44,49] (as illustrated in Fig. 3b and Supplementary Fig. 12a).

Here, we first evaluated the influence of different domains in cells via transient transfection, which focusing mainly on the AH and palmitoylation sites, as the MA loops mutant was hardly expressed in U2OS cells and thus could not be used to measure its association at nanobar-curved membrane sites (Supplementary Fig. 8). Specifically, AH domains have been recognized as typical curvature-sensitive domains widely used by many proteins, including epsin[52], α-Syn[53,54], Arf1[55], and ALPS motifs[54]. Even in alphaviruses, SFV has been reported to contain an AH domain (a.a. 245–264) with a sequence similar to that of CHIKV (a.a. 244–263), and this AH has been shown to both interfere with the membrane-binding affinity of nsP1 in live cells and significantly alter membrane curvature in vitro[20,47,56]. Although the same AH showed less impact on CHIKV membrane binding, whether it alters the sensitivity of nsP1 interacting with curved membranes indirectly is unknown. Here, we tested the AH mutation W258A (nsP1-W258A), which showed impaired membrane binding of nsP1 in SFV[20]. When expressed in cells, nsP1-W258A generated preferential accumulation at the nanobar ends over the bar center (Fig. 3c), despite decreased membrane binding compared to nsP1-WT (Supplementary Fig. 9), consistent with previous studies[47]. The curvature enrichment was similar to that of the wildtype nsP1 (nsP1-WT) with no significant difference in the measured end-to-center ratio (WT: 2.143 ± 1.840 *vs.* W258A: 2.143 ± 1.710, two-tailed unpaired *t* test, $P = 0.9953$) (Fig. 3d). This indicates that the AH domain in nsP1 has indeed a negligible influence on its curvature sensing ability. It is not surprising, as the recent cryo-EM structure of CHIKV nsP1 revealed that the 'AH' (a.a. 244–263) of CHIKV nsP1 was an integral part of the protein core and less likely to be exposed to the membrane for interactions (Fig. 3a)[44], underscoring its minimal impact on curvature sensing ability. These results also presents a non-conventional example that the predicted AH domains from protein sequence analysis might not always contribute to the curvature sensing, depending on the actual protein conformation upon proper folding.

Besides the AH, a palmitoylation-defective mutant at a.a. 417–419 (nsP1-CCC_3A) was also reported to decrease the membrane binding of nsP1 in CHIKV, and its combined double mutation with the AH W258A (nsP1-WCCC_4A) abolished the membrane fraction in cells[47]. When tested on nanobar arrays here, the double mutant nsP1-WCCC_4A produced dominant cytosolic signals with no detectable membrane fraction on the nanobars (Fig. 3c), consistent with earlier reports[47]. The CCC_3A mutant, however, displayed clear enrichment at nanobar ends (Fig. 3c), with a similar end-to-center ratio to nsP1-WT (WT: 2.143 ± 1.840 *vs.* CCC_3A: 2.159 ± 1.702, two-tailed unpaired t-test, $P = 0.8367$) (Fig. 3d), suggesting a non-essential role of palmitoylation in the curvature-guided distribution of nsP1 on the PM. In FRAP tests, nsP1-W258A exhibited no detectable recovery after photobleaching, while nsP1-CCC_3A recovered quickly (Fig. 3e, f and Supplementary Movie 4). It further supports that although palmitoylation may be dispensable for the membrane anchorage of nsP1, it plays a significant role in modulating its mobility on the PM. Overall, neither the AH nor the palmitoylation domain is the major determinant for the curvature sensing of nsP1 in CHIKV.

Besides the AH and palmitoylation, the insertion of the protein's hydrophobic residues has also been reported to contribute to membrane curvature sensing in various proteins, such as the C2 domains of Doc2b and synaptotagmin-1[57,58]. For nsP1, the recent cryo-ET study identified two MA loops that contained four hydrophobic residues at a.a. 220–233 and eight hydrophobic residues at a.a. 407–427 together with the palmitoylation site a.a. 417 to 419 (Fig. 3a)[44,49]. These MA domains are highly conserved among alphaviruses[44]. Here, we evaluated the contribution of the hydrophobic residues from the MA loops on nsP1's curvature sensing. For this purpose, we partially reduced the hydrophobic a.a. in MA loops 1 and 2, as shown in Fig. 3b, and obtained their purified protein from Expi293F cells (eGFP-nsP1-MA loop mut-(m) for short) for in vitro characterization. Negative-staining EM image showed that twelve copies of nsP1 MA loop mutant organized into C12 symmetry, the same as the dodecamer ring observed for WT (Supplementary Fig. 10a)[44]. A gel-based MTase/GTase assay also confirmed the mRNA capping activity of the nsP1 MA loop mutant (Supplementary Fig. 10b). The curvature sensing ability of the nsP1-MA loop mutant was then tested using the nanobar-based SLB assay in vitro. As shown in Fig. 3g, 1 μM eGFP-nsP1-WT-(m) or eGFP-nsP1-MA loop mut-(m) were incubated with 30% POPS SLB. The protein density of nsP1-MA loop mutant bound on nanobars was significantly decreased (0.006 ± 0.003) compared with the nsP1-WT (0.447 ± 0.103) (Fig. 3h), which confirms that the MA loops critical for anchoring nsP1 to membranes. Interestingly, there were two obvious peaks at the curved ends shown in the average image of mammalian expression nsP1 protein, but an even distribution of the mutant around the nanobar (Fig. 3i). The curvature sensitivity of the mutant (1.032 ± 0.139) probed by the end-to-center ratio was significantly lower than the WT (1.134 ± 0.186) at a 300 nm-wide nanobar (Fig. 3j). It suggests that the nsP1-MA loop mutant not only binds less to the membrane but is also less sensitive to curved membranes. Further probing their curvature response on gradient nanobar arrays showed that nsP1 WT exhibited increased protein density at nanobars with end curvature of 500 nm diameter or smaller, while nsP1-MA loop mutant showed much less preference for higher curvature at smaller nanobars (Fig. 3k). This confirms that the hydrophobic residues in the MA loops are critical for nsP1 curvature sensing. Moreover, the impact of curvature-anchoring MA loops on viral replication efficiency was further evaluated using a CHIKV *trans*-replicase system, which contained two plasmids to encode the P1234 polyprotein (or its MA loop mutant) and the RNA replication reporters separately (Fig. 3l and Supplementary Fig. 11). Here, the polyprotein P1234 could be cleaved into the four individual nsPs when expressed in cells. In addition, *firefly* and *Gaussia* luciferase genes were designed as reporters for genomic and subgenomic replication, respectively. Compared with the wild-type nsP1 in P1234 (P1234-WT), the MA loop mutant (P1234-MA-mut) resulted in a significantly decreased expression levels of replication reporters for both genomic and subgenomic regions (Fig. 3m). This confirms the critical role of the MA loops in guaranteeing efficient viral replication.

In addition to hydrophobic insertion, intrinsically disordered regions have recently been shown as new contributors to membrane curvature sensing[59–63]. In nsP1, the entire C-terminal region (a.a. 474–535) has been reported to be disordered (Fig. 3a)[44,49]. To investigate whether it affects the curvature response, we truncated the a.a. from 477–535 at the C-terminal tail (nsP1-(1-476), as shown in Supplementary Fig. 12a). Compared to the wildtype nsP1, nsP1-(1-476) exhibited a much stronger curvature sensing ability with a higher end-

https://doi.org/10.1038/s41467-025-59402-0

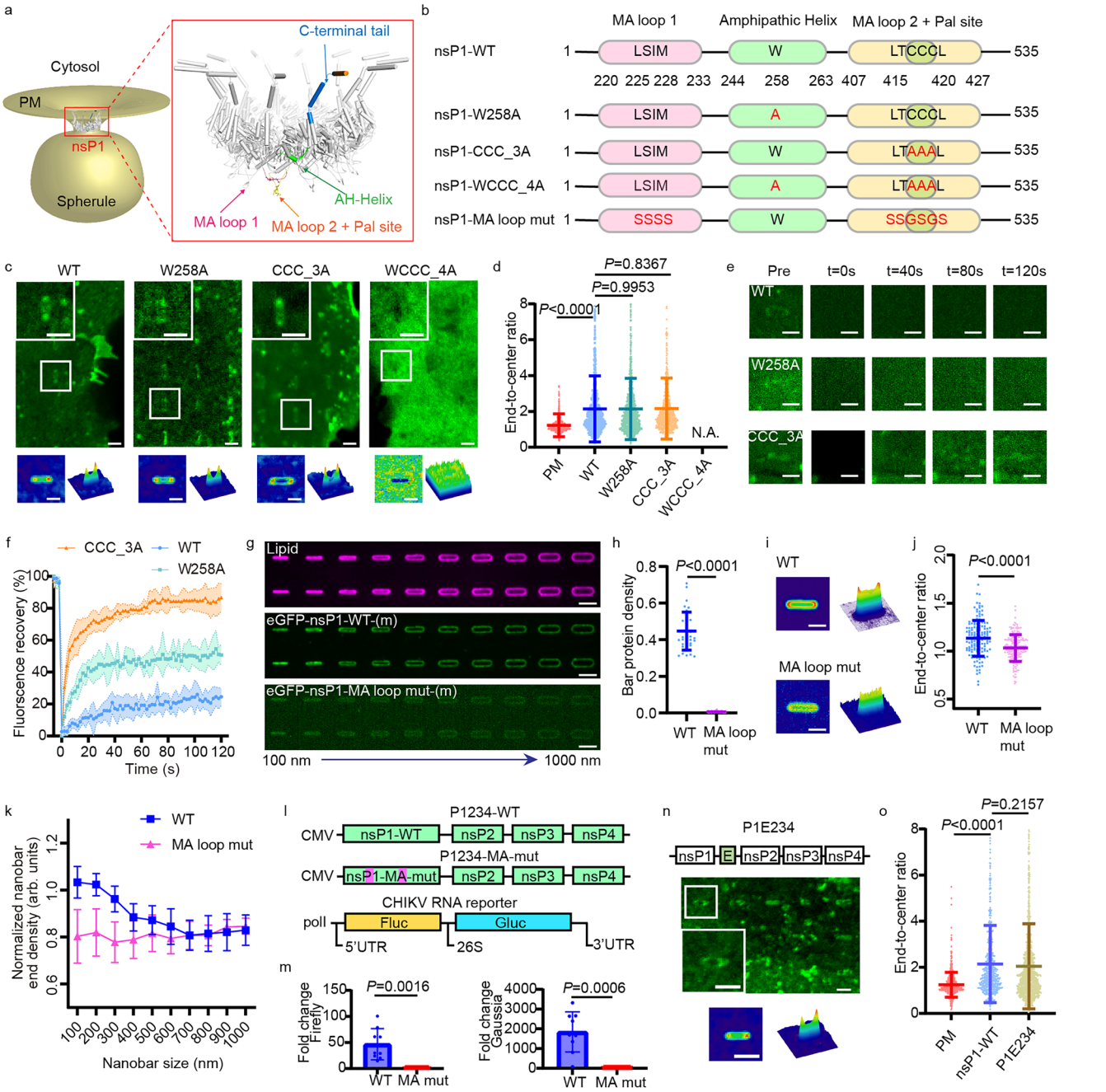

Fig. 3 | Mechanism of CHIKV nsP1 curvature sensing. a Model of nsP1 dodecamer identifying putative membrane binding domains: membrane-association (MA) loops (a.a. 220–233 and 407–427) with a palmitoylation site (a.a. 417–419), one amphipathic helix (AH; a.a. 244–263), and a disordered tail (a.a. 474–535). **b** Mutations of nsP1 used in this study. **c** Confocal images of cells on nanobars expressing eGFP-tagged nsP1-WT, nsP1-W258A, nsP1-CCC_3A, nsP1-WCCC_4A. $n = 3$ repeats. Average images and 3D surface plots are shown below ($n = 291$, 763, 533, 424 bars). **d** The end-to-center ratio of PM, nsP1-WT, nsP1-W258A, nsP1-CCC_3A, nsP1-WCCC_4A on nanobars ($n = 1027$, 1250, 1255, 756). Mean ± SD. **e** Confocal FRAP images of nsP1-WT, nsP1-W258A, nsP1-CCC_3A in 120 s. $n = 3$ repeats. **f** Normalized fluorescence intensity plot of nsP1-WT, nsP1-W258A, nsP1-CCC_3A within the nanobar area from FRAP measurement (2 s interval). Mean ± SD. **g** Confocal images of SLB (magenta) and 1 µM eGFP-tagged mammalian-expressed nsP1-WT (eGFP-nsP1-WT-(m)) or MA-loop-mutant (eGFP-nsP1-MA-loop-mut-(m)) (green) on gradient nanobars. $n = 3$ repeats. **h** Relative protein density of nsP1-WT-(m) ($n = 36$) and nsP1-MA-loop-mut-(m) ($n = 72$). Mean ± SD. **i** Average images and 3D surface plots of nsP1-WT-(m) ($n = 75$ bars) and nsP1-MA-loop-mut-(m) ($n = 93$ bars) on 300 nm-wide nanobars. **j** The end-to-center ratio of nsP1-WT-(m) ($n = 145$) and nsP1-MA loop mut-(m) ($n = 198$) on 300 nm-wide nanobars. Mean ± SD. **k** Normalized nanobar-end density of nsP1-WT-(m) and nsP1-MA loop mut-(m) over 70 bars. Mean ± SEM. **l** Schematic of P1234, its MA-loop-mutant (P1234-MA-mut) and RNA reporter (poll-Fluc-Gluc) constructs. **m** RNA reporter expression level directed by genomic (*firefly* luciferase) and subgenomic (*Gaussia* luciferase) promoters after co-transfection with P1234 or P1234-MA-mut. Mean ± SD. **n** Confocal images of cells expressing eGFP-tagged P1E234 on nanobars. $n = 3$ repeats. Average images and 3D surface plots are shown below ($n = 1103$ bars). **o** The end-to-center ratio of PM, nsP1-WT, P1E234 on nanobars ($n = 666$, 626, 1491). Mean ± SD. Statistical analysis: two-tailed unpaired *t* test. Scale bars: 2 µm. Arb. units = arbitrary units. Source data are provided as a Source Data file.

to-center ratio (WT: 2.039 ± 1.526 *vs.* 1-476: 3.011 ± 3.235, two-tailed unpaired *t* test, $P < 0.0001$) (Supplementary Fig. 12b–d). However, a partial truncation of this disordered region, nsP1-(1-516) (Supplementary Fig. 12a), tuned the curvature response back to the wildtype level (WT: 2.039 ± 1.526 *vs.* 1-516: 2.055 ± 1.428, two-tailed unpaired *t* test, $P = 0.8992$) (Supplementary Fig. 12b–d). It indicates that residues 476 to 516 potentially hinder the nsP1 curvature sensing ability in live cells. One explanation for the decrease in the nsP1 curvature sensing ability when having a.a. 477–516 in live cells is that negatively charged a.a. are dominant in this region (12 vs. 6 among 40 a.a.; Supplementary Fig. 13), which is electrostatically repulsive towards the negatively charged lipid membrane. Another possibility is steric hindrance from the disordered region, which becomes less effective when detached from nsP1.

Beyond the nsP1 protein itself, functional viral replication requires all four nsPs to assemble together to anchor the viral RNA for replication[41]. Whether the binding of other nsPs affects the curvature-promoted nsP1 accumulation was also evaluated by expressing the CHIKV nsP polyprotein P1E234 (with eGFP fused to the C-terminus of nsP1, as illustrated in Fig. 3n) in cells. The results showed an accumulated green fluorescence signal at the nanobar ends (Fig. 3n), suggesting that co-existence and assembly with nsP2, 3, and 4 in cells did not inhibit the curvature preference of nsP1. The measured end-to-center ratio of P1E234 (2.044 ± 1.843) showed no significant difference compared to nsP1-eGFP alone (2.146 ± 1.675, two-tailed unpaired *t* test, $P = 0.2157$) (Fig. 3o). Consistently, the cumulative frequency distribution of P1E234 was indistinguishable from that of the nsP1-WT curve (Supplementary Fig. 14). Hence, the results demonstrate that nsP1 senses and accumulates on curved membrane sites regardless of the binding of other nsPs. On the other hand, other CHIKV nsPs were found to relocate to curved membranes via their association with nsP1. As shown in Supplementary Fig. 15, the sole expression of GFP-tagged nsP3 mainly resulted in fluorescence signals in the cytosol, while co-expression with nsP1 (through P123E4, with GFP fused to the C-terminus of nsP3) resulted in a detectable fraction of nsP3 at the PM.

Validation of curvature-facilitated stabilization of nsP1 via molecular dynamics simulations

To further elucidate the molecular basis of membrane curvature sensing by nsP1, we performed molecular dynamics simulations of nsP1 (a.a. 36–473) on a lipid bilayer containing 20% POPS and 80% POPC. All-atom and coarse-grained simulations were performed to study individual nsP1 molecules and their dodecamer, respectively (Supplementary Fig. 16). For a single copy of the nsP1 molecule on the planar bilayer (Fig. 4a, Supplementary Fig. 17), the MA loop 1 of nsP1 showed charge-dependent binding to the membrane mediated by its positively charged amino acid sidechains and the negatively charged head groups of POPS lipids. However, the MA loop 2 with more hydrophobic residues tended to move away from lipid headgroups, failing to form a stable binding on the membrane. To eliminate the possibility that the initial position of the nsP1 might influence its membrane interaction, we also flipped the nsP1 by 90 degrees and 180 degrees. The results consistently revealed that nsP1 did not form stable binding with the membrane within 20 ns under either configuration (Supplementary Fig. 18). In contrast, nsP1 dodecamer showed significantly stabilized binding to the membrane when introduced in the coarse-grained model (Fig. 4b). After back-mapping[64] the entire nsP1 dodecamer to its all-atom form, we clearly confirmed that binding was through the sequential insertion of nsP1 MA loop 2 into the planar membrane (Fig. 4b, zoom-in area in the black box). Furthermore, the binding of the nsP1 dodecamer generated local positive membrane curvature on the initially flat membrane surface (Supplementary Movie 5). As clearly demonstrated in the heat-map plot of the mean membrane curvature (Fig. 4c), positive membrane curvature was generated at the site of MA loop binding and insertion (red-colored region). Such a variation in the membrane curvature was also clearly seen in the cutaway view in the final image of Fig. 4b.

The generation of positive curvature in the unrestricted membrane at the binding sites of the nsP1 dodecamer suggested a more stable binding of the nsP1 dodecamer to a positively curved membrane. To further test this speculation, we simulated the interaction of the nsP1 dodecamer with SLBs with and without curvature (Fig. 4d, e). Although the nsP1 dodecamer could bind to both SLBs through the sequential insertion of hydrophobic loops into the lipid membrane, its binding to the curved membrane (Fig. 4e) was much more efficient than to the flat one (Fig. 4d). While complete binding of the nsP1 ring to the curved membrane occurred within 450 ns of a production run, complete binding to the flat membrane was not achieved even after 1500 ns. The accelerated binding of nsP1 dodecamer to the curved membrane was possibly due to the curvature-induced increase in area per lipid (Fig. 4f) (planar: 0.646 ± 0.0027 *vs.* curved: 0.680 ± 0.0013, two-tailed unpaired *t* test, $P < 0.0001$)[65], which increased the appearance of lipid packing defects and consequently the exposure of hydrophobic lipid tails to hydrophobic MA loops of nsP1. As expected, the nsP1 dodecamer bound more strongly to the curved membrane as indicated by the more negative total interaction energy due to electrostatic and van der Waals interactions between the nsP1 dodecamer and lipid membrane (Fig. 4g) (planar: −5521 ± 354.8 *vs.* curved: −7061 ± 318.1, two-tailed unpaired *t* test, $P < 0.0001$). The stronger binding between the nsP1 dodecamer and the curved membrane was not only due to the higher number of MA loops inserted but also because the MA loops inserted more deeply into the curved membrane (Fig. 4h) (planar: 0.6383 ± 0.068 *vs.* curved: 0.706 ± 0.052, two-tailed unpaired *t* test, $P < 0.0001$). These simulation results prove that positive membrane curvature enhances nsP1 assembly on the membrane by facilitating the insertion of hydrophobic MA loop 2 and speeding up the binding kinetics, which is in good agreement with nanobar curvature-enhanced nsP1 stabilization observed on the cell PM.

Nanostructure enriched production of CHIKV viral genome

An exciting extension of the curvature-facilitated assembly of CHIKV nsPs for replication is the possibility of guiding the spatial distribution of viral RNA genome replication sites on PM using nanostructure arrays. Recent studies indicated that the formation of membrane spherules during successful viral RNA replication served to compensate for the pressure generated by the growing RNA polymers within the confined membrane compartments[2], suggesting that sufficient space is required near replication sites to accommodate membrane spherule growth without high pressure accumulated. In this sense, the nanobar design might not provide enough space nearby to allow relaxation of the membrane tension built up during replication. To address this issue, we designed nanoring arrays where positive curvature could be generated in three places (as shown in Fig. 5a, b): (i) the sidewall of the outer ring, similar to the positive curve generated on nanobar, with almost no space underneath the positively curved membrane; (ii) the top rim of the outer ring, with sharper curvature than the sidewall and similarly no space under it; and (iii) the top rim of the inner ring, with curvature comparable to that of the outer rim but with extensive nearby space, allowing more extension toward the center of the inner rings. Cells expressing eGFP-nsP1 only exhibited enrichment of fluorescence signal at the positively curved top rim of the ring as well as the outer side of the rings, confirming its positive curvature sensing, similar to its enhanced distribution at the curved nanobar ends (Supplementary Fig. 19). To determine whether nanorings could guide CHIKV replication, we cultured CHIKV-infected cells on nanoring arrays and observed significant enrichment of double-stranded RNA (dsRNA) replication (Fig. 5c and Supplementary Fig. 20), together with nsP1 and nsP3 (Fig. 5d), in the center of the nanoring. In contrast, the replication sites of infected cells on flat surfaces were more randomly distributed throughout the PM (Fig. 5c and

https://doi.org/10.1038/s41467-025-59402-0

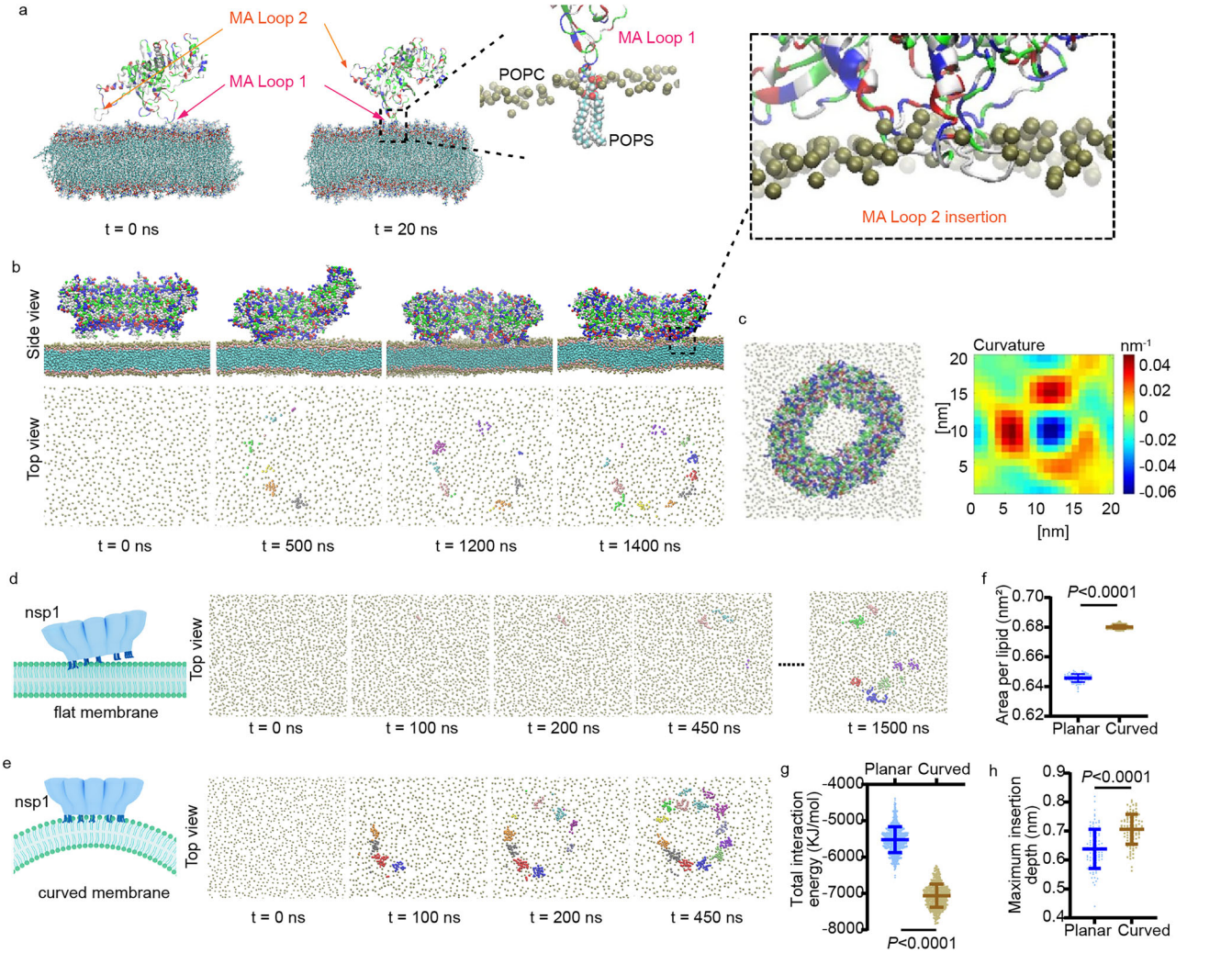

Fig. 4 | Molecular dynamic (MD) simulations of nsP1 protein-lipid membrane interaction. a Snapshots of all-atom MD simulation showing the interaction of a single nsP1 protein with a planar membrane at initial (left) and equilibrated (right) states. Protein atoms are colored by residue type (acidic: red; basic: blue; hydrophobic: white; and polar: green). Lipid atoms are shown as carbon (C; cyan), oxygen (O; red), phosphorus (P; green), nitrogen (N; blue), and hydrogen (H; white). **b** Simulation snapshots showing the temporal evolution of nsP1 dodecamer binding to a planar membrane. The top panels show side cutaway views of nsP1 dodecamer-membrane interaction at different time points; the bottom panels highlight the number of nsP1 ring subunits inserted into the membrane. Lipid head beads (PO4, NC3, and CNO) were colored in tan, glycerol linkages (GL1 and GL2) in pink, lipid tail beads in cyan, and only PO4 beads were shown in the top views. Protein beads in the top panels were colored as in (**a**). The inserted protein beads shown in the bottom panels were rendered in such a way that each color refers to a particular subunit of the dodecamer structure. A zoomed-in box shows the insertion of nsP1 MA loop 2 into the membrane. **c** Top view of the planar membrane-bound nsP1 dodecamer (left) and the corresponding color map for mean membrane curvature (right). **d**, **e** Simulation snapshots showing the temporal evolution of the interaction of the nsP1 dodecamer with a flat supported membrane (**d**) and a supported membrane with a radius of curvature of 100 nm (**e**). **f** Comparison in the area per lipid between planar ($n = 100$) and curved ($n = 191452$) membranes. Mean ± SD. **g** Comparison in the total interaction energy of the nsP1 dodecamer with planar ($n = 981$) and curved ($n = 501$) membranes. Mean ± SD. **h** Comparison in the maximum insertion depth of nsP1 subunits (averaged over all inserted subunits) into planar and curved membranes ($n = 100$). Mean ± SD. Statistical analysis: two-tailed unpaired t test. Source data are provided as a Source Data file.

Supplementary Fig. 20). By measuring the dsRNA signal per unit membrane area, marked by PM staining, we found that dsRNA density inside each ring was significantly elevated compared to the nearby flat area (Fig. 5e). By averaging nanorings with a gradient of inner ring diameters (from 1500 nm to 700 nm, with over 30 rings each), we observed significant accumulation of dsRNA within the inner ring space, with higher dsRNA enrichment in larger rings (Fig. 5f). Two possible factors may contribute to this correlation with inner ring diameter: the longer rim of the positively curved inner ring that could be measured by the inner rim perimeter, and the larger inner ring space proportional to the inner ring area. The contribution of the curved membrane and the nearby space could be compared by normalizing the dsRNA intensity with the inner ring area and perimeter, respectively (Fig. 5g, h). Interestingly, a positive correlation between dsRNA accumulation and inner ring diameter was observed in both cases, indicating that both the existence of the curved membrane and the availability of nearby space are beneficial for viral RNA replication.

The detailed arrangement of viral RC spherules on nanorings was further visualized at high resolution using expansion microscopy (ExM) (Fig. 6a, Supplementary Fig. 21 and Supplementary Movie 6). As shown in Fig. 6b, c, although the curvature-enhanced distribution of nsP1 appeared both surrounding the outer sidewalls of the nanoring and following the rims as expected, successful viral genome replication, marked by dsRNA staining, exhibited dominant accumulation only near the inner ring rim. A zoomed-in view of the inner ring rim (Fig. 6c and Supplementary Fig. 22) further revealed that the dsRNA signals protruded toward the center space of the inner ring, while nsP1 localized at the edge of the dsRNA puncta next to the nanoring rim

https://doi.org/10.1038/s41467-025-59402-0

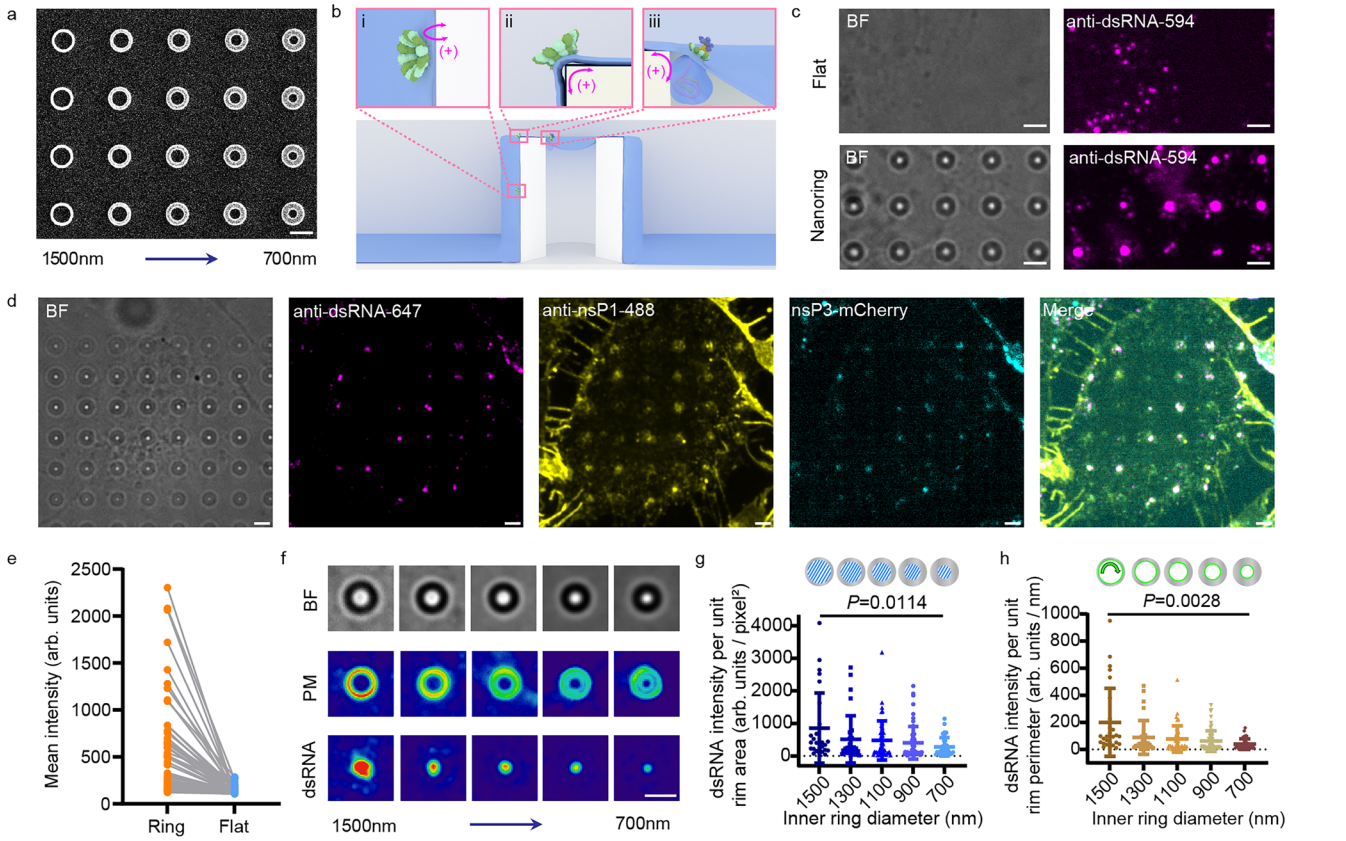

Fig. 5 | Nanostructure guided CHIKV replication. a SEM image of gradient nanorings with decreasing inner ring diameters, ranging from 1500 nm to 700 nm. $n = 3$ repeats. **b** Schematic of a nanoring illustrating three distinct positive curvatures on PM: (i) the sidewall of the outer ring; (ii) the top rim of the outer ring; and (iii) the top rim of the inner ring. **c** Confocal images of CHIKV-infected cells cultured on a flat surface or a nanoring array. Replication sites were indicated by dsRNA staining (magenta). $n = 3$ repeats. **d** Confocal images of nsP3-mCherry tagged CHIKV-infected cells cultured on the nanoring array. The mCherry fluorescent tag was inserted at the hypervariable region of nsP3 (as shown in cyan), which is known to tolerate tags and does not impede virus replication and infection. The cells were stained for nsP1 (yellow) and dsRNA (magenta). $n = 3$ repeats. **e** Comparison of the dsRNA density in the inner ring of the nanoring area and on the nearby flat surface ($n = 60$ rings). **f** Average images of the brightfield, PM intensity, and dsRNA intensity on different-sized nanorings (over 30 rings for each size). **g** The dsRNA intensity per unit inner rim area on different-sized nanorings ($n = 27, 31, 44, 60, 39$). Mean ± SD. **h** The dsRNA intensity per unit inner rim perimeter on different-sized nanorings ($n = 27, 31, 44, 60, 39$). Mean ± SD. Statistical analysis: two-tailed unpaired t-test. Scale bars: 2 μm. Arb. units = arbitrary units. Source data are provided as a Source Data file.

marked by gelatin staining. It confirmes that both curvature-guided nsP1 distribution and nearby space are important for productive viral replication. In addition to the center space of the rings, the bottom of the outer ring also created available space for membrane spherule generation when cells did not wrap the nanoring too tightly, thus also allowing productive RNA replication as marked by dsRNA staining (Fig. 6e). Further zooming in on individual dsRNA puncta confirmed that there were nsP1s localized at their edges and attached to the positively curved outer ring sidewall as well (Fig. 6f and Supplementary Fig. 23). Interestingly, this bottom enrichment of dsRNA was observed only in samples with poor gelatin coating around nanorings (Fig. 6d) but was absent in samples with tighter gelatin coating where no space was detected at the bottom of the nanorings. It further validated that sufficient space is required to allow membrane spherule generation for viral RNA replication.

Overall, by designing nanostructures to decouple the saddle curvature into separate positive and negative curvatures, we revealed that nsP1 formulated an efficient viral protein system to modulate saddle curvatures formed on CHIKV membrane spherules during viral genome replication. As illustrated in Fig. 6g, the MA loops of individual nsP1 can sense a wide range of positive curvatures generated in the x-z plane of the membrane spherule neck, which indeed undergoes a progressive increase during viral replication[2,14]. On the other hand, the dodecamer ring of nsP1 poses a fixed negative curvature in the x-y plane of the neck to prevent fluctuation of the channel opening and to regulate transport during the enlargement of the spherules along with viral genome replication, which also offers a stable anchorage for nsP2, nsP3, and nsP4 to the center of the ring-opening, regardless of the replication-induced changes in positive curvature in the x-z plane[2,14,66]. Distinct from the saddle curvature sensing proteins and peptides reported earlier[35,67–71], the saddle curvature modulation of nsP1 decouples the monomer-based sensing of positive curvature from the oligomer-based generation of negative curvatures into two perpendicular planes. Moreover, our study also demonstrated a potential functional correlation between viral replication and membrane curvature adaptation, where curved membrane sites on PM could effectively guide the spatial distribution of CHIKV replication, thanks to the curvature sensitivity of nsP1. Beyond this study, we envision the crucial role of the membrane shape in viral replication is not only limited to CHIKV replication, but is applicable to other membrane-associated viral replication compartments and the related non-structural proteins from more viruses, such as ZIKV NS1 and hepatitis C virus (HCV) NS4B and NS5B, which have been reported to induce membrane deformation during viral replication[27,72]. In addition, the nanostructure-based assays developed in this study also provide a versatile experimental framework to probe the fundamental principles of membrane remodeling across diverse viral families that replicate within diverse membrane organelles, such as the ER and Golgi[73–75].

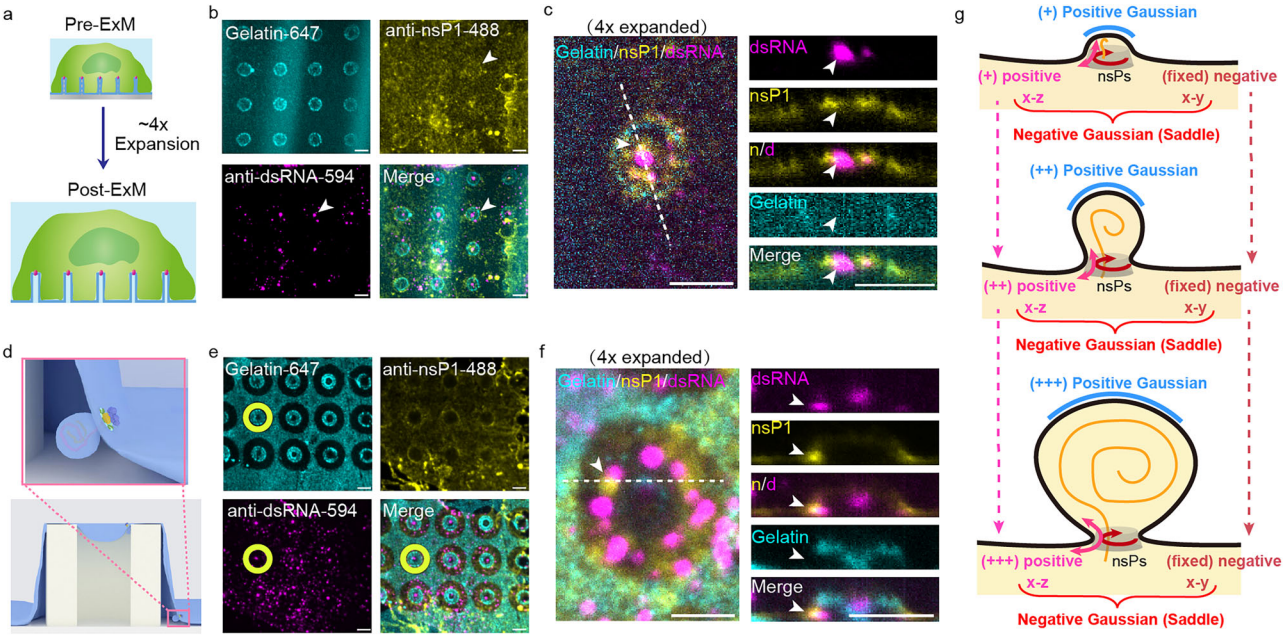

Fig. 6 | Detailed arrangement of the viral replication complex on nanorings revealed by super-resolution imaging. a Schematic of expansion microscopy (ExM) for higher-resolution imaging. **b** Post-ExM images of a CHIKV-infected cell cultured on fluorescent gelatin-coated nanorings (cyan). The cell was stained for nsP1 (yellow) and dsRNA (magenta). A representative replication site is indicated by a white arrow. $n = 3$ repeats. **c** Zoomed-in x-y image (left) and resliced *z*-axis image along the white dashed line (right) show one nanoring with uniform gelatin coating (cyan). The CHIKV-infected cell exhibits dsRNA signals concentrated in the center of the inner ring (magenta), while nsP1 is located at the periphery of the dsRNA puncta near the nanoring rim (yellow). $n = 3$ repeats. **d** Schematic of a nanoring showing that the incomplete PM adhesion to the nanoring sidewall can create space at the bottom of the outer ring, allowing CHIKV replication in this region. **e** Post-ExM images of a CHIKV-infected cell cultured on fluorescent gelatin-coated nanorings (cyan). Incomplete PM adhesion, indicated by dark voids in the gelatin coating around the nanoring (example highlighted by a yellow ring), allows for viral replication within these spaces. The cell was stained for nsP1 (yellow) and dsRNA (magenta). $n = 3$ repeats. **f** Zoomed-in x-y image (left) and resliced *z*-axis image along the white dashed line (right) show replication occurring at the bottom of the outer ring. $n = 3$ repeats. **g** Illustration showing two distinct curvatures generated during spherule formation: 1) a saddle curvature at the neck of the spherule with increasing positive curvature along the x-z plane (pink), sensed by nsP1 via hydrophobic insertion of the MA loops, and a fixed negative curvature along the x-y plane (red) fixed by the size of the nsP1 dodecamer ring; and 2) a progressively increasing positive curvature along the crown of the spherule (blue). Scale bars: 2 μm. Source data are provided as a Source Data file.

Methods

Nanostructure chip fabrication

Nanostructures used in the project were fabricated on quartz wafers (1.5 × 1.5 cm) by the electron-beam lithography (EBL) technique. The quartz chips were first spin-coated with 300 nm positive electron-beam resist PMMA (Allresist, #AR-P672.045), followed by one layer of conductive polymer (Allresist, #AR-PC 5090.02). Customized patterns were exposed by EBL (FEI Helios NanoLab). After that, isopropanol (IPA): methylisobutylketone solution (MIBK, EM Resist, #EMR-P0007001) = 3:1 solution was used to remove the exposed PMMA. Subsequently, a 30 nm chromium (Cr) mask was generated via thermal evaporation (UNIVEX 250 Benchtop) and lift-off in acetone. Nanostructures were finally synthesized through reactive ion etching (RIE) with a mixture of CF_4 and CHF_3 (Oxford Plasmalab 80). SEM (FEI Helios NanoLab) imaging was performed after a 10 nm chromium coating to measure the dimensional properties of nanostructure arrays. Before use, the nanochips were cleaned with Chromium Etchant (Sigma, #651826) to remove the remaining metal layer.

Plasmids

The CHIKV *nsP1* gene was cloned into the vector pEGFP-C1 (Clonetech) following the *eGFP* gene with a tag composed of strep, and the 3 × FLAG tag was inserted after the a.a. 516 residue, referred to as eGFP-nsP1-WT. CHIKV nsP3, P1234-WT, P1E234-WT, P123E4-WT, and RNA reporter (PolI-Fluc-Gluc) plasmids were received as generous gifts from Andres Merits[76]. The VEEV *nsP1* gene was cloned into the same vector as CHIKV *nsP1*. For the generation of the mutants, including CHIKV nsP1-W258A, nsP1-CCC_3A, nsP1-WCCC_4A, nsP1-MA loop mut, P1234-MA-mut, primers were designed to target amino acid residues for mutagenesis. In the case of the plasmids encoding truncated nsP1-(1-476) and (1-516), two stop codons were introduced after residue 476 and residue 516, respectively. Site-directed mutagenesis was performed using the KOD FX Neo polymerase chain reaction kit (TOYOBO) on a thermal cycler. The PCR products were digested with the DpnI restriction enzyme and transformed into DH5-alpha competent *E. coli* cells (New England Biolabs). Transformed cells were plated on kanamycin (50 μg/mL) containing agar plates and incubated overnight at 37 °C. Colonies were selected to grow in LB containing kanamycin (50 μg/mL). Plasmids were recovered with a miniprep kit (Axygen), and successful mutants were identified via Sanger sequencing, which were subsequently used in downstream experiments.

Cell culture on nanostructure array

Homo sapiens bone osteosarcoma U2OS cells (ATCC) were maintained in DMEM with GlutaMAX (Gibco, #10566-016) supplemented medium with 10% fetal bovine serum (FBS) (Gibco, #A5256701) and 1% Penicillin-Streptomycin (PS) (GE Hyclone, #SV30010). One day before transfection or virus infection, cells needed to be cultured onto the nanochip. Before introducing cells to the chip, the surface of the chip needed to be cleaned thoroughly and then underwent high-power air-plasma (Harrick Plasma) treatment for 3 min. After that, the chip was coated with 0.2% gelatin (Sigma, #G9391) for 30 min to facilitate optimal cell adhesion. After coating, the cells were plated onto a 35 mm dish with the nanochip attached to the bottom and waited overnight before transfection or virus infection. The cells were maintained at 37 °C with 5% CO_2.

Cell transfection and membrane staining

Plasmids were transfected with 1 µg plasmid mixed with 1.5 µL Lipofectamine 3000 (Thermo Fisher Scientific, #2713161), 2 µL P3000 reagent (Thermo Fisher Scientific, #2713161), and Opti-MEM (Gibco, #31985-070) and incubated for 30 min. The cells were then starved in Opti-MEM with the plasmid mixture for 4 h, after which they were incubated for 18 h in the DMEM-supplemented medium with 10% FBS and 1% PS to promote protein expression for imaging. CellMask™ Deep Red (Thermo Fisher Scientific, #C10046) staining was performed as a membrane control before imaging. The 1000-fold diluted dye was added to the cells and incubated for 2 min at 37 °C with 5% CO_2. The dye was then washed away with the culture medium to prevent its intake into the cells.

Protein purification

To prepare the bacterial cell expressed CHIKV nsP1, the pNIC-CH2 vector (generous gift from Opher Gileadi, Addgene plasmid #26117) encoding CHIKV nsP1 was transformed into *E.coli* Rosetta 2 (DE3) cells for overexpression[44]. Following induction, the bacterial culture was harvested and lysed. The CHIKV nsP1 protein was then purified from the supernatant using HisPur™ Ni-NTA Resin (Thermo Fisher Scientific) and further purified by size-exclusion chromatography using a HiLoad® 16/600 Superdex® 200 pg column (GE Healthcare Life Sciences)[44]. The monomer fraction was collected and subsequently labeled with Alexa 488 using Alexa Fluor™ 488 Protein Labeling Kit (Invitrogen™) as per the manufacturer's instructions. For the mammalian expression system, plasmids were transfected into Expi293F cells by PEI MAX® (Polysciences) for transient expression. Protein expression was boosted by 10 mM sodium butyrate 16–20 h after transfection. Cell pellets were harvested after 96 h and lysed in the lysis buffer (50 mM Tris-HCl pH 8.0, 150 mM NaCl, 0.5 mM TCEP with protease inhibitor, 1% n-dodecyl-β-D-maltoside (DDM), and 70 mU/mL of BioLock solution (IBA Lifesciences)). The pellet was incubated at 4 °C for 2 h on a rotator with occasional vortexing to ensure complete suspension of the pellet in the lysis buffer. It was subsequently sonicated for 10 min and centrifuged for 1 h at 18,000 g at 4 °C. The supernatant was applied to an Econo-Pac® chromatography column (Biorad) containing Strep-Tactin® Sepharose beads (IBA Lifesciences). After serial washing with 5, 25, and 50 column volumes with the wash buffer (50 mM Tris-HCl pH 8.0, 150 mM NaCl, 0.5 mM TCEP, 10% glycerol), the proteins were eluted using the wash buffer with added 10 mM D-biotin (IBA Lifesciences). The elutants were further purified through Superose® 6 increased 10/300 GL (GE Healthcare Life Sciences) or concentrated to the desired concentration for downstream experiments.

Liposome preparation

The lipid used to test nsP1 curvature sensing consisted of 89.5 mol% Egg PC (L-α-phosphatidylcholine (Egg, Chicken), Avanti, #840051), 0.5 mol% Texas-Red-PE (Texas Red™ 1,2-Dihexadecanoyl-sn-Glycero-3-Phosphoethanolamine, Triethylammonium Salt, Thermo Fisher Scientific, #T1395MP) and 10 mol% Brain PS (L-α-phosphatidylserine (Brain, Porcine) (sodium salt), Avanti, #840032). The lipid used to study the POPS lipid charge effect on nsP1 curvature sensing consisted of POPC (1-palmitoyl-2-oleoyl-glycero-3-phosphocholine, Avanti, #850457), 0.5 mol% Texas-Red-PE with increasing mol% POPS (1-palmitoyl-2-oleoyl-sn-glycero-3-phospho-L-serine (sodium salt), Avanti, #840034) from 0 mol%, 30 mol% to 50 mol%. The lipid used to study the PA lipid charge effect on nsP1 curvature sensing consisted of POPC, 0.5 mol% Texas-Red-PE with increasing mol% PA (1-palmitoyl-2-oleoyl-sn-glycero-3-phosphate (sodium salt), Avanti, #840857) from 0 mol%, 10 mol% to 30 mol%. To study the effect of MA loops on eGFP-nsP1-(m) curvature sensing, a lipid consisting of 69.5 mol% POPC, 0.5 mol% Texas-Red-PE, and 30 mol% POPS was used.

For liposome formation, the lipid mixture with the desired composition was dissolved in chloroform and dried in a brown glass vial under 99.9% nitrogen gas for 5 min, followed by vacuum drying for at least 3 h to remove the remaining chloroform. The dried mixture was then resuspended in phosphate buffered saline (PBS, Gibco, #70013-032) buffer to achieve a concentration of 2 µg/µL and sonicated for 30 min. This was followed by a freeze-thaw cycle performed 20 times (20 s in liquid nitrogen, 2 min in a 42 °C water bath) until the lipid mixture became clear. Subsequently, the mixture was extruded using an extruder equipped with a holder/heating block (Sigma, #610000-1EA), passing through a 100 nm pore-size polycarbonate membrane 20 times until the solution appeared clearer. The resulting lipid vesicle solution was collected and stored at 4 °C in preparation for SLB formation.

Supported lipid bilayer formation on nanochips

The nanochips were first cleaned with piranha solution (1 part 30% hydrogen peroxide solution and 7 parts concentrated sulfuric acid) overnight. Afterward, the chips were rinsed with a continuous stream of deionized water, dried with 0.45 µm-filtered 99.9% nitrogen gas, and hydrophilized and cleaned with high-power air-plasma (Harrick Plasma) treatment for 1 h. Lipid vesicles were then loaded onto the well-cleaned nanochips. The chips were attached to a polydimethylsiloxane (PDMS) chamber to prevent the lipids from drying. After a 15 min incubation, excess lipid vesicles were washed away with 200 µL PBS buffer five times to form the lipid bilayer. Subsequently, the protein solution was added to the lipid-bilayer-coated nanochips, incubated for 15 min, and prepared for fluorescence imaging.

Negative staining electron microscopy (EM) sample preparation and microscopy

Briefly, copper grids (Carbon Film 300 Mesh Cu, Electron Microscopy Sciences) were glow-discharged for 45 s and prepared with 10 µL of purified protein sample. After 1 min incubation, the excess sample was removed with filter paper, and 2% uranyl acetate stain (Electron Microscopy Sciences) was applied for 1 min with excess stain removed with filter paper. Negative-stained samples were screened on a Thermo Fisher FEI Tecnai T12 microscope at 120 kV with an Eagle camera.

RNA 5′ end capping assay

This method was previously described by Li et al.[77] and optimized for CHIKV nsP1 by Law et al.[78]. The CHIKV 5′ UTR sequence was used as the template to synthesize the substrate RNA. The 5′ triphosphorylated (ppp) single-stranded 12-mer RNA AUGGCUGCGUGA labeled with a fluorescein amidite (FAM) dye was named "pppAU-10 FAM". A 5′ diphosphorylated (pp) single-stranded 12-mer RNA, AUGGCUGCGUGA, was labeled with a FAM dye at the 3′ end and named "ppAU-10 FAM". A Cap-0 RNA was synthesized based on the above sequence and named "m^7GpppAU-10", or, when labeled with a FAM dye, "m^7GpppAU-10 FAM", respectively. In addition, 5′ triphosphorylated (ppp) single-stranded 12-mer RNA AGUUGUUAGUCU, based on the dengue virus 5′ UTR labeled with FAM dye, was named "pppAG-10 FAM", and a Cap-0 RNA was named "m^7GpppAG-10 FAM". The RNAs were synthesized by Trilink Biotechnologies and Bio-Synthesis Inc. The capping reaction was performed in two steps. Firstly, a covalent nsP1-m^7GMP intermediate reaction was prepared in a 20 µL containing 20 µM nsP1, 50 mM Tris-HCl (pH 7.5), 2 mM dithiothreitol (DTT), 10 mM KCl, and 2 mM $MgCl_2$ and 0.5 mM S-adenosylmethionine (SAM) and 1 mM GTP or an alternative substrate as cap donor, and incubated at 30 °C for 2 h. Secondly, the covalent m^7GMP-nsP1 was used for transfer to the RNA recipient in a 20 µL mixture containing 5 µL covalent intermediate, 50 mM Tris-HCl pH 7.5, 2 mM DTT, 2 mM $MgCl_2$, 1 µM synthetic RNA, and 20 U Murine RNase Inhibitor (New England Biolabs). The reactions were incubated at 30 °C for 12 h and terminated by adding the stop

solution (2 × RNA loading dye: 95% formamide, 0.02% bromophenol blue, 0.01% xylene cyanol, 0.02% sodium dodecyl sulfate (SDS), 1 mM ethylenediaminetetraacetic acid (EDTA)). The capped RNA products were separated by 20% denaturing RNA 8 M urea polyacrylamide gel electrophoresis (PAGE) gel and visualized using ChemiDoc™ MP imaging system (Biorad).

The *trans*-replicase system for analyzing CHIKV replicase activities

HEK293FT cells were maintained in DMEM with GlutaMAX supplemented medium with 10% FBS and 1% PS at 37 °C with 5% CO_2. Cells grown in 24-well plates were co-transfected with 0.5 μg of plasmid encoding RNA reporter (polI-Fluc-Gluc) with 0.5 μg of CMV-P1234 or CMV-P1234-MA-mutant by PEI MAX® (Polysciences). CMV: immediate early promoter of human cytomegalovirus; polI: truncated promoter for human or *Aedes albopictus* RNA polymerase; Fluc: *firefly* luciferase; Gluc: *Gaussia* luciferase. After 24 hours of incubation, the cells were washed with PBS and lysed. The expression levels of firefly and Gaussia luciferase were measured using the Dual-Luciferase® Reporter Assay System (Promega) on a 96-well plate (Corning) with a microplate reader (Synergy™ H1, BioTek). The activities of the RNA reporters were normalized to control cells transfected with the sole RNA reporter.

CHIKV infection in cells

U2OS cells were cultured on the nanochip one day before CHIKV infection. On the day of infection, cells were washed once in 1 × PBS and infected with CHIKV WT or nsP3-mCherry tagged CHIKV at MOI = 1 in RPMI 1640 medium containing 2% FBS and incubated for 1 h with occasional rocking. Virus-containing medium was removed and replaced with fresh RPMI 1640 medium containing 2% FBS. After 24 h of infection, the cells were washed three times with pre-warmed PBS and fixed with 4% paraformaldehyde (PFA, Tousimis, #1008 A) for 15 min. After washing with PBS for three times, the cells were then permeabilized with 0.5% Triton X-100 (Sigma, T8787) in PBS for 15 min and blocked using 5% bovine serum albumin (BSA) (Sigma, #A9647) in PBS for 1 h. Subsequently, the samples were stained with anti-dsRNA (1:200, SCICONS, #10010500) and anti-nsP1 (1:200, a gift from Andres Merits) at room temperature for 1 h, and then washed three times with PBS, followed by staining with the secondary antibodies anti-mouse IgG Alexa 594 (1:200, Thermo Fisher Scientific, #A32744) and anti-rabbit IgG Alexa 488 (1:200, Thermo Fisher Scientific, #A32731) at room temperature for 1 h. The samples were then washed three times with PBS for subsequent imaging.

Expansion microscopy (ExM) on nanostructure array

The ExM sample preparation followed a modified version of the protocol described by Tillberg et al.[79] and Nakamoto et al.[80]. To make the cell membrane wrap tightly around the nanostructure, the surface of the nanochip was first cleaned with high-power air-plasma (Harrick Plasma) treatment for 1 h and then coated with 50 μg/mL poly-L-lysine (PLL, Sigma, #25988-63-0) for 20 min, 0.5% glutaraldehyde (Sigma, #G7651) for 30 min and 0.02 mg/mL gelatin (Sigma) labeled with Atto647N-NHS ester (Sigma, #18373) for 40 min. For poor gelatin coating around the nanostructure, as shown in Fig. 5k, l, plasma cleaning was not necessary. U2OS cells were then cultured on the nanochips. After CHIKV infection and immunostaining, the cells were incubated overnight at 4 °C in a 1:100 dilution of Acryloy-X (Thermo Fisher Scientific, #A2077) in PBS. Subsequently, the cells were incubated in the gelation solution (monomer solution (8.6% (w/w) Sodium acrylate (Sigma, #408212), 2.5% (w/w) Acrylamide (Sigma, #A8887), 0.15% (w/w) N, N′-Methylenebis (acrylamide) (Sigma, #146072)) with 0.2% Tetramethylethylenediamine (TEMED, Bio-Rad, #1610801), 0.01% 4-Hydroxy-TEMPO (Sigma, #176141) and 0.2% Ammonium persulfate (APS, Sigma, #A3678) at 4 °C overnight. Afterward, the nanochip with the hydrogel was incubated in digestion buffer (50 mM Tris HCl, 1 mM EDTA, 0.5% Triton X-100, 1 M NaCl) with a 1: 100 diluted proteinase K (Sigma, #P4850). After 2 h of incubation at room temperature, the hydrogel was detached from the nanochip. The hydrogel was then incubated overnight in MiliQ water at 4 °C. Before imaging, the hydrogel was carefully transferred to a PLL-coated glass bottom dish with a few drops of MiliQ water to maintain humidity.

Microscopy imaging

Imaging of transfection results in live cells, time series of nsP1 dynamics in live cells, bacterial expressed nsP1 monomer (eGFP-nsP1-(b)) distributed on SLB nanobar structures, and the related FRAP tests were performed with laser scanning confocal microscopy (Zeiss LSM 800 with Airyscan) with a 100x/1.4 oil objective. For live cell imaging, the cells were maintained in live cell imaging solution (Thermo Fisher Scientific, #A59688DJ) at 37°C in an on-stage incubator. For in vitro SLB imaging, free chips were attached to a polydimethylsiloxane (PDMS) chamber. EGFP and Alexa Fluor™ 488-labeled nsP1 were excited at 488 nm and detected at 490–570 nm. Texas-Red-PE containing lipid bilayer was excited at 561 nm and detected at 570-645 nm. CellMask™ Deep Red was excited at 633 nm and detected at 645–700 nm. Each image had a resolution of 512 × 512 pixels, with a pixel size of 124 nm and a bit depth of 16. The scanning speed was 20 s/image with an averaging mode of 4 times/line. For time series imaging, the scanning speed was 1 s/image without the averaging mode. For FRAP imaging, a circular area containing one nanobar was selected and bleached with a laser. FRAP videos were collected at 1 s/image without averaging mode.

STED super-resolution imaging of nsP1 in cells was performed with a STEDYCON scanner (Abberior Instruments) with 488, 561, and 640 nm excitation lasers together with a 775 nm STED laser (all pulsed). The STEDYCON was mounted to a Nikon Ti2 inverted microscope with a 100x/1.45 oil objective. Before imaging, the cells were stained with an nsP1-specific antibody, followed by a STAR RED (Abberior) secondary antibody, and finally mounted with MOUNT medium (Abberior).

Imaging of the FRAP test of nsP1 and its mutations around nanobars in live cells, the lipid charge effect, the IDR (a.a. 477–516) effect on bacterial expressed nsP1 curvature sensing, the distributions of mammalian expressed nsP1 and its MA loops mutations on SLB-nanobar structures, and CHIKV infection in cells around nanostructures with or without ExM were performed with a spinning disc confocal microscope (SDC) that built around a Nikon Ti2 inverted microscope equipped with a Yokogawa CSU-W1 confocal spinning head and a 100x/1.4 oil objective. EGFP was excited at 488 nm and detected at 490–570 nm. CellMask™ Deep Red was excited at 639 nm and detected at 672–712 nm. Each image had a resolution of 1152 × 1152 pixels, with a pixel size of 65 nm. For FRAP imaging, a circular area containing one nanobar was selected and bleached with a laser. FRAP videos were collected at 2 s/image.

Image analysis and quantification

To quantify the protein membrane curvature response in live cells, the end-to-center ratio was calculated using ImageJ and MATLAB code. In brief, the background of each individual nanobar image was first corrected by subtracting the local background with the rolling ball algorithm in ImageJ (radius = 3 pixels for 250 nm diameter nanobars). Next, the individual nanobar position was identified using a square mask that defined the end area and center area. Nanobars with signals from random protein aggregation or with undetectable protein signals were excluded from further analysis. To minimize human bias, all parameters for the calculation and the sorting criteria for data validation were kept consistent. The average intensity values from each square mask were used to generate the average images. The intensity values of pixels within each end and center area were extracted to calculate the end-to-center ratio. The kymograph and the migration of nsP1 protein clusters were manually tracked using

ImageJ, and the protein migratory behavior was characterized using a computer program called DiPer[81]. To generate the FRAP recovery curve, the FRAP area was selected using ImageJ, and the intensity was plotted over time with bleaching correction. The membrane binding abilities between nsP1-WT and nsP1-W258A were compared by drawing a line profile from the background to the cytosol of the cell and plotting the intensity along this line using ImageJ. The intensity was then normalized from 0 to 100, and the mean normalized intensity at each position was plotted.

For in vitro SLB assay curvature sensing quantification, we first located the square mask for individual nanobars. After that, the background of each nanobar image was subtracted using the meshgrid function in MATLAB based on the four ROIs at the corners of the image to correct for surface unevenness. The average images and end-to-center ratios were then collected as described for the live cell assay. For gradient nanobar quantification, the intensities of background-corrected individual nanobar images of different sizes were first normalized to the percentage of the largest-sized nanobar center intensity to decrease the batch variation. Protein density was measured by the ratio of normalized protein intensity to normalized lipid intensity. The nanobar end areas were adjusted according to the dimension of each nanobar to minimize the covering of the nearby non-curved center in order to obtain the normalized nanobar end density.

The density of dsRNA within the inner ring of the nanoring was quantified by measuring the dsRNA signal per unit membrane area, marked by PM staining. The nearby flat area was located 40 pixels to the right of each inner ring. For different-sized inner rings, the dsRNA intensity per unit area was quantified by measuring the integrated dsRNA signal within the inner ring and dividing it by the corresponding inner ring area. Similarly, the dsRNA intensity per unit perimeter was calculated by dividing the dsRNA signal by the respective rim perimeter. Statistical analysis was performed by PRISM 9 (GraphPad).

Molecular dynamics simulations of nsP1 protein-lipid membrane interaction

Simulation of nsP1 monomer-membrane interaction. The interaction between a single copy of the nsP1 protein and a planar membrane was modeled using all-atom and coarse-grained molecular dynamics (MD) simulations. For the all-atom simulation, the atomic coordinates of the nsP1 monomer were taken from the dodecamer structure in the Protein Data Bank (code 7DOP)[44]. The missing residues (366–375, 415–418, and 452–458) in the nsP1 monomer structure were modeled using DaReUs-Loop Webserver[82]. Missing residues 31 to 35 could not be modeled by the web server, so the first 35 residues were omitted from the model, as they form an independent segment that is distal from the MA loops and also not involved in the inter-monomer interface. The 3D model was then placed in a simulation box with TIP3P water molecules and neutralizing chloride ions under 3D periodic boundary conditions. MD simulations were next performed using GROMACS version 2018.2 with the all-atom CHARMM27 forcefield[83–85]. Visual Molecular Dynamics (VMD) software version 1.9.4 was used for visualization[86]. After energy minimization and equilibration with positional restraints on non-H atoms, an unrestrained simulation was performed for 5 ns with a 2 fs time-step to equilibrate the nsP1 monomer in water. The temperature was maintained at 303 K, and the pressure was maintained at 1 bar. Electrostatic interactions were computed using the Particle Mesh Ewald method with a cut-off distance of 1.2 nm. Van der Waals (vdW) interactions were computed using a cut-off method with forces smoothly switched to zero between 1.0 and 1.2 nm.

The equilibrated nsP1 monomer structure was then placed on top of an equilibrated planar membrane composed of 80% POPC and 20% POPS lipids. The lipid membrane was built using Bilayer Membrane Builder in CHARMMM-GUI webserver[87], consisting of 230 lipids per leaflet. The system was solvated with TIP3P water molecules and with 3D periodic boundary conditions imposed. Sodium and chloride ions were added to electrically neutralize the system. The CHARMM36m force field was used to describe inter-atomic interactions. Energy minimization was then performed to avoid any clashes between the molecules, followed by equilibration of the system for 2 ns at 310 K and 1 bar. Three independent simulations were carried out for 20 ns each by assigning different sets of initial velocities to the atoms (Supplementary Fig. 24).

To analyze the interactions between the nsP1 monomer and the lipid membrane over longer time scales, coarse-grained simulations were performed. For coarse-grained simulations, the lipid membrane, along with water and ions, were coarse-grained with the help of martinize script following the MARTINI model of coarse-graining[88]. The nsP1 protein was coarse-grained separately and then placed over the lipid membrane. After setting up the initial configuration, the system was energy minimized, followed by equilibration for 5 ns. The production run was carried out for 300 ns, with the temperature maintained at 310 K and the pressure maintained at 1 bar. The velocity-rescale method was used for temperature coupling, while pressure coupling was performed using the Berendsen method and Parrinello-Rahman method during equilibration and production run, respectively. The simulations were repeated three times with different initial velocities assigned to coarse-grained beads, similar to all-atom simulations discussed above.

Simulation of nsP1 dodecamer-membrane interaction. Further, the interaction between the nsP1 dodecamer and planar membrane was analyzed using coarse-grained MD simulation for computational efficiency. Firstly, the complete nsP1 monomer model was fitted to each of the 12 subunits in the dodecamer to obtain a complete all-atom model. Next, a coarse-grained nsP1 dodecamer structure was obtained based on the MARTINI coarse-grained model using the *martinize* script version 2.6.3[88]. The coarse-grained nsP1 dodecamer was then placed on top of a planar lipid membrane (2000 lipids) with POPC:POPS lipids (80%:20%) in the upper leaflet using the CHARMM-GUI interface. The lipid membrane was modeled using the MARTINI 3.0 forcefield[89]. After energy minimization, equilibration for 5 ns was conducted at 310 K and 1 bar, followed by a production run for 1400 ns at the same temperature and pressure. To quantify changes to the membrane curvature upon nsP1 ring binding, the *g_lomepro* tool downloaded from http://www3.mpibpc.mpg.de/groups/de_groot/g_lomepro.html was used to obtain the local mean membrane curvature[90]. Simulation snapshots from 1360 to 1400 ns (40 frames), during which the nsP1 ring was stably bound to the membrane, were used for the analysis. A band-pass filter ($q_{low} = 0.3\ nm^{-1}$ and $q_{high} = 0.7\ nm^{-1}$) was applied to the computed curvature modes so as to capture the strongly curved region of the membrane. Finally, simulations were set up to analyze the binding affinity of the nsP1 dodecamer towards SLBs with and without curvature. A flat membrane and a curved one with a radius of curvature of 100 nm were set up following the protocol by Liu et. al.[91]. In brief, the lipid head beads in the inner leaflet were fixed with the help of a restraining force constant of $1000\ kJ\ mol^{-1}\ nm^{-2}$. The simulations were conducted using a coarse-grained MD simulation technique with the MARTINI 3.0 forcefield and similar conditions as mentioned in previous coarse-grained planar membrane simulations. Finally, it's the total interaction energy between the nsP1 dodecamer and with both planar and curved membranes. This is one of the commonly used methods to quantify the binding strength between different molecules of interest[92–95]. In addition, the insertion depths of MA loops in the planar and curved membranes were quantified with the help of a TCL script.

Statistical analysis

At least three independent experiments were used to perform the statistical analysis. Statistical differences were assessed using a two-tailed unpaired *t* test with Welch's correction. Statistical analyses

were conducted using Prism 9.0 software for Windows (GraphPad Software, San Diego, CA). *P*-values are indicated in the figure legends, and a *P*-value of < 0.05 was considered statistically significant. All microscopy images shown are representative of at least three independent experiments.

Reporting summary

Further information on research design is available in the Nature Portfolio Reporting Summary linked to this article.

Data availability

The figure data generated in this study have been deposited in the DR-NTU database at https://doi.org/10.21979/N9/INZ1S1. All data that support this work are included in the Article, the Supplementary Information, and the Source Data files. Source data are provided in this paper.

Code availability

The code for the analysis is deposited in a Zenodo repository. (https://doi.org/10.5281/zenodo.15117231).

References

1. Ferraris, P. et al. Sequential biogenesis of host cell membrane rearrangements induced by hepatitis C virus infection. *Cell. Mol. Life Sci.* **70**, 1297–1306 (2013).
2. Laurent, T. et al. Architecture of the chikungunya virus replication organelle. *ELife* **11**, e83042 (2022).
3. Welsch, S. et al. Composition and three-dimensional architecture of the dengue virus replication and assembly sites. *Cell Host Microbe* **5**, 365–375 (2009).
4. Cortese, M. et al. Ultrastructural characterization of zika virus replication factories. *Cell Rep.* **18**, 2113–2123 (2017).
5. Knoops, K. et al. SARS-coronavirus replication is supported by a reticulovesicular network of modified endoplasmic reticulum. *PLoS Biol.* **6**, e226 (2008).
6. Eymieux, S. et al. Ultrastructural modifications induced by SARS-CoV-2 in Vero cells: a kinetic analysis of viral factory formation, viral particle morphogenesis and virion release. *Cell. Mol. Life Sci.* **78**, 3565–3576 (2021).
7. Miller, S. & Krijnse-Locker, J. Modification of intracellular membrane structures for virus replication. *Nat. Rev. Microbiol.* **6**, 363–374 (2008).
8. Thaa, B. et al. Differential phosphatidylinositol-3-kinase-Akt-mTOR activation by semliki forest and Chikungunya viruses is dependent on nsP3 and connected to replication complex internalization. *J. Virol.* **89**, 11420–11437 (2015).
9. Bienz, K., Egger, D. & Pasamontes, L. Association of polioviral proteins of the P2 genomic region with the viral replication complex and virus-induced membrane synthesis as visualized by electron microscopic immunocytochemistry and autoradiography. *Virology* **160**, 220–226 (1987).
10. Miller, D. J., Schwartz, M. D. & Ahlquist, P. Flock house virus RNA replicates on outer mitochondrial membranes in Drosophila cells. *J. Virol.* **75**, 11664–11676 (2001).
11. Froshauer, S., Kartenbeck, J. & Helenius, A. Alphavirus RNA replicase is located on the cytoplasmic surface of endosomes and lysosomes. *J. Cell Biol.* **107**, 2075–2086 (1988).
12. Magliano, D. et al. Rubella virus replication complexes are virus-modified lysosomes. *Virology* **240**, 57–63 (1998).
13. McCartney, A. W., Greenwood, J. S., Fabian, M. R., White, K. A. & Mullen, R. T. Localization of the tomato bushy stunt virus replication protein p33 reveals a peroxisome-to-endoplasmic reticulum sorting pathway. *Plant Cell* **17**, 3513–3531 (2005).
14. Tan, Y. B. et al. Molecular architecture of the Chikungunya virus replication complex. *Sci. Adv.* **8**, eadd2536 (2022).
15. Netherton, C., Moffat, K., Brooks, E. & Wileman, T. A guide to viral inclusions, membrane rearrangements, factories, and viroplasm produced during virus replication. *Adv. Virus Res.* **70**, 101–182 (2007).
16. Cho, M. W., Teterina, N., Egger, D., Bienz, K. & Ehrenfeld, E. Membrane rearrangement and vesicle induction by recombinant poliovirus 2C and 2BC in human cells. *Virology* **202**, 129–145 (1994).
17. Zimmermann, L. et al. SARS-CoV-2 nsp3 and nsp4 are minimal constituents of a pore spanning replication organelle. *Nat. Commun.* **14**, 7894 (2023).
18. Yu, L., Takeda, K. & Gao, Y. Characterization of virus-specific vesicles assembled by West Nile virus non-structural proteins. *Virology* **506**, 130–140 (2017).
19. Kumar, S. et al. Chikungunya virus nsP1 interacts directly with nsP2 and modulates its ATPase activity. *Sci. Rep.* **8**, 1045 (2018).
20. Spuul, P. et al. Role of the amphipathic peptide of Semliki forest virus replicase protein nsP1 in membrane association and virus replication. *J. Virol.* **81**, 872–883 (2007).
21. Kaufusi, P. H., Kelley, J. F., Yanagihara, R. & Nerurkar, V. R. Induction of endoplasmic reticulum-derived replication-competent membrane structures by West Nile virus non-structural protein 4B. *PLoS ONE* **9**, e84040 (2014).
22. Miller, S., Kastner, S., Krijnse-Locker, J., Bühler, S. & Bartenschlager, R. The non-structural protein 4A of dengue virus is an integral membrane protein inducing membrane alterations in a 2K-regulated manner. *J. Biol. Chem.* **282**, 8873–8882 (2007).
23. Hung, Y.-F. et al. Amino terminal region of dengue virus NS4A cytosolic domain binds to highly curved liposomes. *Viruses* **7**, 4119–4130 (2015).
24. Hung, Y.-F. et al. Dengue virus NS4A cytoplasmic domain binding to liposomes is sensitive to membrane curvature. *Biochim. Biophys. Acta* **1848**, 1119–1126 (2015).
25. Gottipati, K., Woodson, M. & Choi, K. H. Membrane binding and rearrangement by chikungunya virus capping enzyme nsP1. *Virology* **544**, 31–41 (2020).
26. Varkey, J. et al. An Amphipathic Alpha-Helix Domain from Poliovirus 2C Protein Tubulate Lipid Vesicles. *Viruses* **12**, https://doi.org/10.3390/v12121466 (2020).
27. Ci, Y. et al. Zika NS1-induced ER remodeling is essential for viral replication. *J. Cell Biol.* **219**, https://doi.org/10.1083/jcb.201903062 (2020).
28. Zhao, W. et al. Nanoscale manipulation of membrane curvature for probing endocytosis in live cells. *Nat. Nanotechnol.* **12**, 750–756 (2017).
29. Lou, H.-Y. et al. Membrane curvature underlies actin reorganization in response to nanoscale surface topography. *Proc. Natl. Acad. Sci. USA* **116**, 23143–23151 (2019).
30. Mu, H. et al. Patterning of oncogenic ras clustering in live cells using vertically aligned nanostructure arrays. *Nano Lett.* **22**, 1007–1016 (2022).
31. El Alaoui, F. et al. Structural organization and dynamics of FCHo2 docking on membranes. *ELife* **11**, https://doi.org/10.7554/eLife.73156 (2022).
32. Cail, R. C., Shirazinejad, C. R. & Drubin, D. G. Induced nanoscale membrane curvature bypasses the essential endocytic function of clathrin. *J. Cell Biol.* **221**, e202109013 (2022).
33. Lu, C.-H. et al. Membrane curvature regulates the spatial distribution of bulky glycoproteins. *Nat. Commun.* **13**, 3093 (2022).
34. Zhang, W. et al. Curved adhesions mediate cell attachment to soft matrix fibres in three dimensions. *Nat. Cell Biol.* **25**, 1453–1464 (2023).
35. Brunetti, R. M. et al. WASP integrates substrate topology and cell polarity to guide neutrophil migration. *J. Cell Biol.* **221**, https://doi.org/10.1083/jcb.202104046 (2022).

36. Rosholm, K. R. et al. Membrane curvature regulates ligand-specific membrane sorting of GPCRs in living cells. *Nat. Chem. Biol.* **13**, 724–729 (2017).
37. Breuer, A., Lauritsen, L., Bertseva, E., Vonkova, I. & Stamou, D. Quantitative investigation of negative membrane curvature sensing and generation by I-BARs in filopodia of living cells. *Soft Matter* **15**, 9829–9839 (2019).
38. Yang, S. et al. Membrane curvature governs the distribution of Piezo1 in live cells. *Nat. Commun.* **13**, 7467 (2022).
39. Ledoux, B. et al. Plasma membrane nanodeformations promote actin polymerization through CIP4/CDC42 recruitment and regulate type II IFN signaling. *Sci. Adv.* **9**, eade1660 (2023).
40. Spuul, P., Balistreri, G., Kääriäinen, L. & Ahola, T. Phosphatidylinositol 3-kinase-, actin-, and microtubule-dependent transport of Semliki Forest Virus replication complexes from the plasma membrane to modified lysosomes. *J. Virol.* **84**, 7543–7557 (2010).
41. Rana, J. et al. Network mapping among the functional domains of Chikungunya virus nonstructural proteins. *Proteins* **82**, 2403–2411 (2014).
42. Ahola, T., Lampio, A., Auvinen, P. & Kääriäinen, L. Semliki Forest virus mRNA capping enzyme requires association with anionic membrane phospholipids for activity. *EMBO J* **18**, 3164–3172 (1999).
43. Aïqui-Reboul-Paviet, O. et al. The Rac1-PAK1-Arp2/3 signaling axis regulates CHIKV nsP1-induced filopodia and optimal viral genome replication. *J. Virol.* **98**, e0061224 (2024).
44. Zhang, K. et al. Structural insights into viral RNA capping and plasma membrane targeting by Chikungunya virus nonstructural protein 1. *Cell Host Microbe* **29**, 757–764 (2021).
45. Strauss, J. H. & Strauss, E. G. The alphaviruses: gene expression, replication, and evolution. *Microbiol. Rev.* **58**, 491–562 (1994).
46. Kim, D. Y. et al. New world and old world alphaviruses have evolved to exploit different components of stress granules, FXR and G3BP proteins, for assembly of viral replication complexes. *PLoS Pathog.* **12**, e1005810 (2016).
47. Bakhache, W., Neyret, A., Bernard, E., Merits, A. & Briant, L. Palmitoylated cysteines in Chikungunya virus nsP1 are critical for targeting to cholesterol-rich plasma membrane microdomains with functional consequences for viral genome replication. *J. Virol.* **94**, https://doi.org/10.1128/jvi.02183-19 (2020).
48. Bigay, J. & Antonny, B. Curvature, lipid packing, and electrostatics of membrane organelles: defining cellular territories in determining specificity. *Dev. Cell* **23**, 886–895 (2012).
49. Jones, R., Bragagnolo, G., Arranz, R. & Reguera, J. Capping pores of alphavirus nsP1 gate membranous viral replication factories. *Nature* **589**, 615–619 (2021).
50. Jumper, J. et al. Highly accurate protein structure prediction with AlphaFold. *Nature* **596**, 583–589 (2021).
51. Frost, A. et al. Structural basis of membrane invagination by F-BAR domains. *Cell* **132**, 807–817 (2008).
52. Capraro, B. R., Yoon, Y., Cho, W. & Baumgart, T. Curvature sensing by the epsin N-terminal homology domain measured on cylindrical lipid membrane tethers. *J. Am. Chem. Soc.* **132**, 1200–1201 (2010).
53. Jensen, M. B. et al. Membrane curvature sensing by amphipathic helices: a single liposome study using α-synuclein and annexin B12. *J. Biol. Chem.* **286**, 42603–42614 (2011).
54. Pranke, I. M. et al. α-Synuclein and ALPS motifs are membrane curvature sensors whose contrasting chemistry mediates selective vesicle binding. *J. Cell Biol.* **194**, 89–103 (2011).
55. Lundmark, R., Doherty, G. J., Vallis, Y., Peter, B. J. & McMahon, H. T. Arf family GTP loading is activated by, and generates, positive membrane curvature. *Biochem. J.* **414**, 189–194 (2008).
56. Lampio, A. et al. Membrane binding mechanism of an RNA virus-capping enzyme. *J. Biol. Chem.* **275**, 37853–37859 (2000).
57. Groffen, A. J. et al. Doc2b is a high-affinity Ca2+ sensor for spontaneous neurotransmitter release. *Science* **327**, 1614–1618 (2010).
58. Hui, E., Johnson, C. P., Yao, J., Dunning, F. M. & Chapman, E. R. Synaptotagmin-mediated bending of the target membrane is a critical step in Ca(2+)-regulated fusion. *Cell* **138**, 709–721 (2009).
59. Davidson, W. S., Jonas, A., Clayton, D. F. & George, J. M. Stabilization of alpha-synuclein secondary structure upon binding to synthetic membranes. *J. Biol. Chem.* **273**, 9443–9449 (1998).
60. Bigay, J., Casella, J.-F., Drin, G., Mesmin, B. & Antonny, B. ArfGAP1 responds to membrane curvature through the folding of a lipid packing sensor motif. *EMBO J.* **24**, 2244–2253 (2005).
61. Zeno, W. F. et al. Synergy between intrinsically disordered domains and structured proteins amplifies membrane curvature sensing. *Nat. Commun.* **9**, 4152 (2018).
62. Yamamoto, H., Kondo, A. & Itoh, T. A curvature-dependent membrane binding by tyrosine kinase Fer involves an intrinsically disordered region. *Biochem. Biophys. Res. Commun.* **495**, 1522–1527 (2018).
63. Su, M. et al. Comparative study of curvature sensing mediated by F-BAR and an intrinsically disordered region of FBP17. *iScience* **23**, 101712 (2020).
64. Wassenaar, T. A., Pluhackova, K., Böckmann, R. A., Marrink, S. J. & Tieleman, D. P. Going backward: A flexible geometric approach to reverse transformation from coarse grained to atomistic models. *J. Chem. Theory Comput.* **10**, 676–690 (2014).
65. Chng, C.-P., Sadovsky, Y., Hsia, K. J. & Huang, C. Curvature-regulated lipid membrane softening of nano-vesicles. *Extreme Mech. Lett.* **43**, https://doi.org/10.1016/j.eml.2021.101174 (2021).
66. Kril, V. et al. Alphavirus nsP3 organizes into tubular scaffolds essential for infection and the cytoplasmic granule architecture. *Nat. Commun.* **15**, 8106 (2024).
67. Schmidt, N. W. et al. Criterion for amino acid composition of defensins and antimicrobial peptides based on geometry of membrane destabilization. *J. Am. Chem. Soc.* **133**, 6720–6727 (2011).
68. Hu, K. et al. A critical evaluation of random copolymer mimesis of homogeneous antimicrobial peptides. *Macromolecules* **46**, 1908–1915 (2013).
69. Schmidt, N. W., Mishra, A., Wang, J., DeGrado, W. F. & Wong, G. C. L. Influenza virus A M2 protein generates negative Gaussian membrane curvature necessary for budding and scission. *J. Am. Chem. Soc.* **135**, 13710–13719 (2013).
70. Pipathsouk, A. et al. The WAVE complex associates with sites of saddle membrane curvature. *J. Cell Biol.* **220**, https://doi.org/10.1083/jcb.202003086 (2021).
71. Pfitzner, A.-K. et al. An ESCRT-III Polymerization sequence drives membrane deformation and fission. *Cell* **182**, 1140–1155 (2020).
72. Romero-Brey, I. et al. Three-dimensional architecture and biogenesis of membrane structures associated with hepatitis C virus replication. *PLoS Pathog.* **8**, e1003056 (2012).
73. Arakawa, M. & Morita, E. Flavivirus replication organelle biogenesis in the endoplasmic reticulum: Comparison with other single-stranded positive-sense RNA viruses. *Int. J. Mol. Sci.* **20**, https://doi.org/10.3390/ijms20092336 (2019).
74. Stancheva, V. G. & Sanyal, S. Positive-strand RNA virus replication organelles at a glance. *J. Cell Sci.* **137**, https://doi.org/10.1242/jcs.262164 (2024).
75. Sandoval, I. V. & Carrasco, L. Poliovirus infection and expression of the poliovirus protein 2B provoke the disassembly of the Golgi complex, the organelle target for the antipoliovirus drug Ro-090179. *J. Virol.* **71**, 4679–4693 (1997).
76. Utt, A. et al. Design and use of Chikungunya virus replication templates utilizing mammalian and mosquito RNA polymerase

I-mediated transcription. *J. Virol.* **93**, https://doi.org/10.1128/jvi.00794-19 (2019).
77. Li, C. et al. mRNA Capping by venezuelan equine encephalitis virus nsP1: Functional characterization and implications for antiviral research. *J. Virol.* **89**, 8292–8303 (2015).
78. Law, M. C. Y., Zhang, K., Tan, Y. B., Nguyen, T. M. & Luo, D. Chikungunya virus nonstructural protein 1 is a versatile RNA capping and decapping enzyme. *J. Biol. Chem.* **299**, 105415 (2023).
79. Tillberg, P. W. et al. Protein-retention expansion microscopy of cells and tissues labeled using standard fluorescent proteins and antibodies. *Nat. Biotechnol.* **34**, 987–992 (2016).
80. Nakamoto, M. L., Forró, C., Zhang, W., Tsai, C.-T. & Cui, B. Expansion microscopy for imaging the cell-material interface. *ACS Nano* **16**, 7559–7571 (2022).
81. Gorelik, R. & Gautreau, A. Quantitative and unbiased analysis of directional persistence in cell migration. *Nat. Protoc.* **9**, 1931–1943 (2014).
82. Karami, Y. et al. DaReUS-Loop: a web server to model multiple loops in homology models. *Nucleic Acids Res.* **47**, W423–W428 (2019).
83. Abraham, M. J. et al. GROMACS: High performance molecular simulations through multi-level parallelism from laptops to supercomputers. *SoftwareX* **1–2**, 19–25 (2015).
84. Lindahl, E., Hess, B. & van der Spoel, D. GROMACS 3.0: a package for molecular simulation and trajectory analysis. *J. Mol. Model.* **7**, 306–317 (2001).
85. Lee, J. et al. CHARMM-GUI Input generator for NAMD, GROMACS, AMBER, OpenMM, and CHARMM/OpenMM simulations using the CHARMM36 additive force field. *J. Chem. Theory Comput.* **12**, 405–413 (2016).
86. Humphrey, W., Dalke, A. & Schulten, K. VMD: visual molecular dynamics. *J. Mol. Graph.* **14**, 33–38 (1996).
87. Jo, S., Kim, T., Iyer, V. G. & Im, W. CHARMM-GUI: a web-based graphical user interface for CHARMM. *J. Comput. Chem.* **29**, 1859–1865 (2008).
88. de Jong, D. H. et al. Improved parameters for the MARTINI coarse-grained protein force field. *J. Chem. Theory Comput.* **9**, 687–697 (2013).
89. Souza, P. C. T. et al. Martini 3: a general purpose force field for coarse-grained molecular dynamics. *Nat. Methods* **18**, 382–388 (2021).
90. Gapsys, V., de Groot, B. L. & Briones, R. Computational analysis of local membrane properties. *J. Comput. Aided Mol. Des.* **27**, 845–858 (2013).
91. Liu, J. et al. Membrane packing defects in synaptic vesicles recruit complexin and synuclein. *Phys. Chem. Chem. Phys.* **23**, 2117–2125 (2021).
92. Ma, Y. et al. Novel linear peptides with high affinity to αvβ3 integrin for precise tumor identification. *Theranostics* **7**, 1511–1523 (2017).
93. Loschwitz, J. et al. Novel inhibitors of the main protease enzyme of SARS-CoV-2 identified via molecular dynamics simulation-guided in vitro assay. *Bioorg. Chem.* **111**, 104862 (2021).
94. Todde, G. & Friedman, R. Conformational modifications induced by internal tandem duplications on the FLT3 kinase and juxtamembrane domains. *Phys. Chem. Chem. Phys.* **21**, 18467–18476 (2019).
95. Irvine, W. A., Flanagan, J. U. & Allison, J. R. Computational prediction of amino acids governing protein-membrane interaction for the PIP3 cell signaling system. *Structure* **27**, 371–380 (2019).

Acknowledgements

We thank Dr. Andres Merits (University of Tartu, Estonia) for providing anti-nsP1 antibody, CHIKV P1234 plasmid, and HSPolI-Fluc-Gluc plasmid; Dr. Yee-Song Law (Lee Kong Chian School of Medicine, NTU) for constructing eGFP-nsP1 plasmid and purifying bacterial expressed nsP1 proteins; Ms. Sin Yi Chong (School of Chemistry, Chemical Engineering and Biotechnology, NTU) for maintaining cells during the early stage of this project. We thank the Nanyang NanoFabrication Center (N2FC) and the Center for Disruptive Photonic Technologies (CDPT) at Nanyang Technological University (NTU) for supporting nanostructure fabrication and SEM imaging; the School of Chemistry, Chemical Engineering and Biotechnology NTU and Dr. Yansong Miao (School of Biological Science, NTU) for generous support on the laser scanning and the spinning disk confocal microscopes. We thank the financial support provided by the China Scholarship Council (CSC) and the guidance of Dr. Junxian Yun (College of Chemical Engineering, Zhejiang University of Technology) for Dr. Jiawei Wu's work. This work was supported by funding from the Singapore Ministry of Education under its MOE Academic Research Fund Tier 3 Awards MOET32020-0001 and MOET32023-0004 (to W.Z.), Tier 2 Awards MOE-T2EP30222-0022 (to W.Z.), MOE-T2EP30220-0009 (to D.L.), MOE-T2EP30124-0023 (to D.L.), MOE-T2EP50121-0004 (to C.H.) and Tier 1 grants RG112/20 (to W.Z.), RG95/21 (to W.Z.), RG93/22 (to W.Z.), RG84/21 (to D.L.), RT22/23 (to D.L.); National Research Foundation under NRF-MSG-2023-0001 (to W.Z.) and NRF/ASTAR quantum engineering program NRF2021-QEP2-03-P10 (to W.G.); Human Frontier Science Program under Early-Career Research Grant (RGY0088/2021) (to W.Z.). We would also like to acknowledge the support received from the Ministry of Education, Singapore, under its Research Center of Excellence award to the Institute for Digital Molecular Analytics (IDMxS, grant: EDUN C-33-18-279-V12) (to W.Z.), and Nanyang Technological University for its Start-Up Grant (to W.Z.). The computational work for this article was fully performed on the resources of the National Supercomputing Center, Singapore (https://www.nscc.sg).

Author contributions

X.M., D.L., and W.Z. conceived the study and designed the experiment. X.M. performed most of the experiments. M.L. purified the mammalian-expressed nsP1 proteins and conducted the virus infection experiment. J.K., C.C., and C.H. performed the molecular simulation analysis. Y.P.Z., X.G., Y.Y.Z., and W.G. fabricated the nanostructures, performed SEM imaging, and tested the chips. M.L. and Y.T. performed TEM measurements. X.M. and J.W. analyzed most of the data. X.M. and L.H. performed the expansion microscopy. X.M. and W.Z. drafted the manuscript. All the authors discussed the results and commented on the manuscript. Project administration and funding acquisition: W.Z., D.L., C.H., and W.G.

Competing interests

The following authors declare competing interests: W.Z., D.L., and X.M. are listed as inventors on a patent application (10202500872Q) filed by Nanyang Technological University, related to an anti-viral drug screening platform. The remaining authors declare no competing interests.

Additional information

Supplementary information The online version contains supplementary material available at https://doi.org/10.1038/s41467-025-59402-0.

Correspondence and requests for materials should be addressed to Changjin Huang, Dahai Luo or Wenting Zhao.

Peer review information *Nature Communications* thanks Tero Ahola, and the other anonymous reviewer(s) for their contribution to the peer review of this work. A peer review file is available.